Astronomy & Astrophysics manuscript no. Paper_final_arXiv
September 22, 2016
©ESO 2016

An all-sky census of Galactic high-latitude molecular intermediate-velocity clouds ⋆

T. Röhser[1], J. Kerp[1], D. Lenz[1], and B. Winkel[2]

[1] Argelander-Institut für Astronomie (AIfA), Universität Bonn, Auf dem Hügel 71, D-53121 Bonn
e-mail: troehser@astro.uni-bonn.de
[2] Max-Planck-Institut für Radioastronomie (MPIfR), Auf dem Hügel 69, D-53121 Bonn

Received —; accepted —

arXiv:1609.06540v1 [astro-ph.GA] 21 Sep 2016

ABSTRACT

Context. The H I halo clouds of the Milky Way and in particular the intermediate-velocity clouds (IVCs) are thought to be connected to Galactic fountain processes. Observations of fountain clouds are important for understanding the role of matter recycling and accretion onto the Galactic disk and subsequent star formation.
Aims. Here, we quantify the amount of molecular gas in the Galactic halo. We focus on the rare class of molecular IVCs (MIVCs) and search for new objects.
Methods. The H I-FIR correlation is studied across the entire northern and southern Galactic hemispheres at Galactic latitudes $|b| > 20°$ in order to determine the amount and distribution of molecular gas in IVCs. We use the most recent large-scale H I and FIR data, the Effelsberg Bonn-H I Survey, the Parkes Galactic All-Sky Survey, and the *Planck* FIR surveys.
Results. We present a catalogue of 239 MIVC candidates on the northern and southern Galactic hemispheres. Among these candidates all previously known MIVCs are recovered except for a single one only. The frequency of candidates differs significantly between the northern and southern Galactic hemispheres and between negative and positive LSR velocities as well.
Conclusions. In our approach we analyse the local Galactic environment. Extrapolating to the entire Galaxy, the global inflow of atomic and molecular IVC gas onto the Milky Way may account for the major fraction of the gaseous mass needed for sustaining the current Galactic star formation rate.

Key words. Galaxy: halo – ISM: clouds – ISM: molecules – catalogs

1. Introduction

A star forming galaxy such as the Milky Way requires the continuous accretion of matter in order to sustain its star formation activity over time scales of Gyrs (e.g. Fraternali & Tomassetti 2012; Putman et al. 2012). The accreted material needs to be of low metallicity in order to match the observed abundances in Galactic stellar populations, which is known as the G-dwarf problem (Alibés et al. 2001). Gaseous halos of galaxies are thought to be an important reservoir for such material (e.g. Wakker 2001).

The intermediate- and high-velocity clouds (IVCs and HVCs) are prominent structures of extra-planar cold, atomic gas in our Galaxy (Putman et al. 2012, for a recent review on gaseous halos). These classes of H I halo clouds are defined by their anomalous radial velocity that is incompatible with simple rotation models. IVCs are typically defined with $40\,\mathrm{km\,s^{-1}} \leq |v_{\mathrm{LSR}}| \leq 90\,\mathrm{km\,s^{-1}}$, HVCs with $90\,\mathrm{km\,s^{-1}} \leq |v_{\mathrm{LSR}}|$ (e.g. Wakker 2001).

The IVCs are located within a distance of ∼2 kpc consisting of near solar metallicity gas. The HVCs have distances of $5 \lesssim D \lesssim 20\,\mathrm{kpc}$ and lower metallicities (e.g. Wakker 2001). A major exception is the Magellanic System, which is located at much larger distance (e.g. Nidever et al. 2010). Commonly, FIR emission is detected towards IVCs (Planck Collaboration XXIV 2011), however, so far no dust emission could be convincingly associated with HVCs (Wakker & Boulanger 1986; Planck Collaboration XXIV 2011; Williams et al. 2012; Saul et al. 2014; Lenz et al. 2016) or their detection is tentative (Miville-Deschênes et al. 2005; Peek et al. 2009). These properties suggest that IVCs may be connected to a Galactic fountain process while HVCs represent an extragalactic reservoir of gas (e.g. Putman et al. 2012).

According to this picture IVCs are considered as an inflow of gas consisting predominantly of recycled disk material. During the fountain cycle clouds may gain mass by the local cooling of the hot halo medium (Marinacci et al. 2010; Marasco et al. 2012). Hence, as fountain clouds, IVCs may contribute to the global accretion.

Star formation requires cold and dense gas as fuel (e.g. Putman et al. 2012). Such gas may harbour molecules and their presence can be used to identify cold and dense gas. Studies using absorption spectroscopy reveal a widespread distribution of low molecular hydrogen (H_2) column densities of $N_{\mathrm{H_2}} = 10^{14}-10^{16}\,\mathrm{cm^{-2}}$ within IVCs (Richter et al. 2003; Wakker 2006).

There are a few molecular intermediate-velocity clouds (MIVCs) that contain significant amounts of molecular gas such that carbon monoxide ^{12}CO(1→0) emission is detected (Magnani & Smith 2010). These MIVCs are of prime interest for studies of inflowing cold, dense, and molecular material onto the Milky Way (e.g. Miville-Deschênes et al. 2016). MIVCs are located at scale heights of a few hundred parsecs above the disk with in-falling radial velocities (Magnani & Smith 2010). These rare objects are Draco, IVC 135, IVC 210, G 283.8+54.9, G 288.4+53.2, and G 295.0+57.1. The latter three appear to be

⋆ The candidate lists in Tables 5 and 6 are available at the CDS.

part of the same gaseous structure (Magnani & Smith 2010). Because of their large amounts of molecular gas, Draco (Mebold et al. 1985, 1987; Rohlfs et al. 1989; Herbstmeier et al. 1993, 1996; Moritz et al. 1998; Heithausen et al. 2001; Miville-Deschênes et al. 2016), IVC 135 (Weiß et al. 1999; Heithausen et al. 2001; Hernandez et al. 2013; Lenz et al. 2015), and IVC 210 (Désert et al. 1990; Röhser et al. 2014, 2016) have been extensively studied. Furthermore, there are solid distance limits for these three MIVCs (Gladders et al. 1998; Benjamin et al. 1996; Röhser et al. 2014).

The low number of MIVCs suggests that either MIVCs are rare and require special conditions to form or only a small fraction of the MIVC population has been detected so far. The CO survey conducted by Dame et al. (2001) covers only latitudes of $|b| \lesssim 20^\circ$ except for a few known high-latitude molecular structures. The CO maps extracted from the *Planck* surveys (Planck Collaboration XIII 2014) only have a limited sensitivity and do not provide spectral information.

Hence, one has to rely on the indirect inference of molecular hydrogen on Galactic scales. One method is the correlation of H I and FIR dust emission and the analysis of its residuals. With respect to the linear H I-FIR correlation FIR excess is inferred, which is commonly attributed to the presence of molecular hydrogen (Désert et al. 1988; Reach et al. 1998).

The most recent and comprehensive study of FIR-excess emission is conducted by Reach et al. (1998). However, they consider only the total H I column density within $-100\,\mathrm{km\,s^{-1}} \leq v_{\mathrm{LSR}} \leq 100\,\mathrm{km\,s^{-1}}$ and, thus, do not make use of the velocity information of the H I data. In addition, the angular resolution and quality of their data, especially in H I, is surpassed significantly by the new all-sky surveys that are available today (Winkel et al. 2016a; Kalberla & Haud 2015; Planck Collaboration I 2014).

Here, we present an all-sky search for MIVCs focussing on high Galactic latitudes of $|b| > 20^\circ$. At lower latitudes many different gas components are superimposed along the lines-of-sight, which does not allow to reliably disentangle different FIR emission components by their H I counterparts.

This paper is organised as follows. In Sect. 2 we present the H I and FIR data that we use in this all-sky analysis. In Sect. 3 we discuss the H I-FIR correlation and how we estimate H_2 column densities on Galactic scales. In addition, MIVC candidates are defined by a set of observed quantities. In Sect. 4 we present the distribution of the inferred MIVC candidates on the northern Galactic hemisphere at $b > 20^\circ$. In Sect. 5 the same analysis is shown for the southern Galactic hemisphere at $b < -20^\circ$. An additional analysis of the global MIVC samples is presented in Sect. 6. Our results are discussed in Sect. 7 and we conclude in Sect. 8.

2. Data

2.1. H I data

For the atomic hydrogen we combine the most recent large-scale H I surveys to obtain an all-sky coverage. On the northern hemisphere there is the Effelsberg-Bonn H I Survey (EBHIS, Winkel et al. 2016a; Kerp et al. 2011; Winkel et al. 2010), which covers the sky at Declinations of $\delta \geq -5^\circ$ with the Effelsberg 100 m telescope. The data has a half-power beam width of $\theta \simeq 10.8'$ and a spectral channel width of $\Delta v \simeq 1.29\,\mathrm{km\,s^{-1}}$ (Table 1).

The Parkes Galactic All-Sky Survey (GASS, McClure-Griffiths et al. 2009; Kalberla et al. 2010; Kalberla & Haud 2015) is a fully sampled survey of Galactic H I with the Parkes 64 m telescope for Declinations of $\delta \leq 1^\circ$. The angular resolution of the data is $\theta \simeq 16.1'$ with a channel spacing of $\Delta v \simeq 0.82\,\mathrm{km\,s^{-1}}$ (Table 1).

Table 1: Data sets used in this study. The columns give the angular resolution θ, the spectral channel width Δv, and the brightness temperature noise ΔT.

Data	θ [arcmin]	Δv [km s^{-1}]	ΔT [mK]	References
EBHIS	10.8	1.29	90	(1)
GASS	16.1	0.82	57	(2)
Planck τ	5.27	–	–	(3)

References. (1) Winkel et al. (2016a); Kerp et al. (2011); Winkel et al. (2010); (2) McClure-Griffiths et al. (2009); Kalberla et al. (2010); Kalberla & Haud (2015); (3) Planck Collaboration XI (2014).

Both, EBHIS and GASS, are corrected for stray radiation, which is an emission component that enters the receiving system of the telescopes through its sidelobes (Kalberla et al. 1980). The relative contribution to the measured signal is largest at high Galactic latitudes and, thus, has to be removed (e.g. Winkel et al. 2016a, their Fig. A.2.).

Both surveys are combined into a single all-sky H I data set. In order to achieve a uniform coverage, we smooth the EBHIS data to the angular resolution of GASS. Furthermore, the GASS data is smoothed to the spectral resolution of EBHIS. In the overlap region of EBHIS and GASS at $-5^\circ \leq \delta \leq 1^\circ$ the two surveys are averaged. The FITS maps are computed in zenith-equal area projection (Calabretta & Greisen 2002) using the convolution-based gridder *cygrid* (Winkel et al. 2016b).

Additionally, we decompose the EBHIS and GASS data cubes into Gaussian components. This decomposition is achieved by simultaneously fitting a varying number of Gaussian components to each individual spectrum. The Akaike information criterion (Akaike 1974) is used to avoid overfitting by penalising models with more parameters. A maximum number of 15 components per spectrum is fitted. The amplitudes have to be positive and larger than the noise and the line widths have to reflect reasonable gas temperatures for the ISM. These Gaussian components are used for the identification of cold atomic gas (Sect. 3.3). The Gaussian decomposition is not unique. However, narrow and bright line components are identified easily because they dominate the HI emission along their lines-of-sight.

2.2. FIR data

The FIR intensity of dust continuum emission can be described by the spectrum of a modified black-body (e.g. Boulanger et al. 1996). Dust optical depths τ are inferred by Planck Collaboration XI (2014) from data measured by the *Planck* satellite at 353 GHz, 545 GHz, and 857 GHz in addition to the 3000 GHz data from IRIS (Miville-Deschênes & Lagache 2005). The dust models are provided on a HEALPix grid (Górski et al. 2005) at an angular resolution of $5'$. Due to the gridding to FITS[1] maps the angular resolution is degraded slightly (Table 1). The dust optical depths τ are smoothed to the angular resolution of GASS for the H I-τ correlation study and the inference of $N_{\mathrm{H_2}}$. In addition, the point source mask is applied that is derived by Planck Collaboration XXVI (2015) at 857 GHz.

[1] http://fits.gsfc.nasa.gov/

3. Methods

Within the diffuse ISM there is a linear correlation between the total hydrogen column density and the FIR dust emission (e.g. Boulanger et al. 1996). This linear correlation allows the removal of the FIR emission that is associated with the atomic phase (Désert et al. 1988; Reach et al. 1998). The residual emission contains many different contributions, e.g. intrinsic variations of the H I-FIR correlation or variations of the gas-to-dust ratio, or dust that is associated with ionised or molecular hydrogen (e.g. Planck Collaboration XIX 2011). All these effects may cause structured residual FIR emission.

3.1. The H-FIR correlation

The following equations describe the general correlation between gas and dust in the ISM at Galactic coordinates (l, b) (e.g. Lenz et al. 2015; Röhser et al. 2016):

$$\begin{aligned}\tau(l,b) &= R + \epsilon \times N_{\rm H}(l,b) \\ &\simeq R + \epsilon \times \left[N_{\rm H\,II}(l,b) + N_{\rm H\,I}(l,b) + 2N_{\rm H_2}(l,b)\right]. \end{aligned} \quad (1)$$

In this representation there are two linear parameters, the constant offset R and the dust emissivity ϵ. Since we focus here on the inference of molecular hydrogen in IVCs, we consider clouds with H I column densities $N_{\rm H\,I} \geq 1 \times 10^{20}\,{\rm cm^{-2}}$, for which the transition from atomic to molecular hydrogen is observed to occur (e.g. Gillmon et al. 2006). In such environments the ionised hydrogen column density is thought to be negligible (Lagache et al. 2000). The assumption of a single dust emissivity for the atomic and molecular gas is a simplification that ignores detected small variations of dust emission properties even in the diffuse ISM (Ysard et al. 2015; Fanciullo et al. 2015).

The kinematical information on the H I gas is used to differentiate between different gaseous components: low-velocity, intermediate-velocity, and high-velocity clouds (LVCs, IVCs, HVCs). For the LVCs we choose $-20\,{\rm km\,s^{-1}} \leq v_{\rm LSR} \leq +20\,{\rm km\,s^{-1}}$, for the IVCs $20\,{\rm km\,s^{-1}} \leq |v_{\rm LSR}| \leq 100\,{\rm km\,s^{-1}}$, and for the HVCs $100\,{\rm km\,s^{-1}} \leq |v_{\rm LSR}| \leq 450\,{\rm km\,s^{-1}}$. The velocity limit for the distinction between LVC and IVC gas is rather low (e.g. Wakker 2001). However, some of the known high-latitude molecular clouds have radial velocities of about $-25\,{\rm km\,s^{-1}}$, like Draco, G 288.4+53.2, or G 295.0+57.1 (Magnani & Smith 2010). Hence, these objects are included in our IVC definition.

We calculate all-sky H I column density maps of the LVC gas for $-20\,{\rm km\,s^{-1}} \leq v_{\rm LSR} \leq +20\,{\rm km\,s^{-1}}$, negative IVC gas $N_{\rm H\,I}^{\rm IVC^-}$ with $-100\,{\rm km\,s^{-1}} \leq v_{\rm LSR} \leq -20\,{\rm km\,s^{-1}}$, and positive IVC gas $N_{\rm H\,I}^{\rm IVC^+}$ at $+20\,{\rm km\,s^{-1}} \leq v_{\rm LSR} \leq +100\,{\rm km\,s^{-1}}$.

The HVC H I gas is neglected in the H I-τ correlation since it is not associated with detectable amounts of FIR emission (e.g. Planck Collaboration XXIV 2011; Lenz et al. 2016). Hence, the observed dust optical depths τ can be described by a two-component model

$$\tau \simeq R + \epsilon^{\rm LVC} \times (N_{\rm H\,I}^{\rm LVC} + 2N_{\rm H_2}^{\rm LVC}) + \epsilon^{\rm IVC} \times (N_{\rm H\,I}^{\rm IVC} + 2N_{\rm H_2}^{\rm IVC}) \quad (2)$$

that distinguishes between LVCs and IVCs. Both components may have different gas-to-dust ratios expressed as different emissivities ϵ^i (e.g. Planck Collaboration XXIV 2011). If there is FIR excess emission or molecular hydrogen associated with LVCs, these lines-of-sight are difficult to analyse since one cannot distinguish uniquely between excess emission that originates from LVC or IVC gas. Hence, we assume $N_{\rm H_2}^{\rm LVC} \simeq 0$, assigning the entire excess emission to the IVC component. This conclusion is, however, incorrect if there is significant gas and dust emission associated with the LVC regime. Consequently, these regions are excluded from the further analysis to a large extent in our definition of MIVCs (Sect. 3.3).

Rearranging Eq. (2) yields

$$N_{\rm H_2}^{\rm IVC} \simeq \frac{1}{2}\left(\frac{\tau - (R + \epsilon^{\rm LVC} \times N_{\rm H\,I}^{\rm LVC})}{\epsilon^{\rm IVC}} - N_{\rm H\,I}^{\rm IVC}\right), \quad (3)$$

allowing to estimate H_2 column densities within IVCs across large angular scales.

3.2. Fitting the H I-τ correlation

The parameters R, $\epsilon^{\rm LVC}$, and $\epsilon^{\rm IVC}$ are obtained from fits of Eq. (2) to the *linear* part of the H-τ correlation, which is assumed to be dominated by atomic hydrogen. However, at some threshold H I column density the atomic hydrogen turns molecular introducing the non-linear FIR excess that steepens the linear H I-τ correlation (Désert et al. 1988). The H I-H_2 transition is smooth and continuous (compare with Fig. 1).

In order to quantify the non-linear contribution of H_2 to the H-τ correlation, we apply the iterative fitting method as described by Röhser et al. (2016). The two-component model (Eq. 2) is fitted below an upper H I column density threshold of $4 \times 10^{20}\,{\rm cm^{-2}}$ in either LVC or IVC H I column density.

We fit the two-component model separately for the entire northern and southern Galactic hemispheres with $b > 20°$ or $b < -20°$ to determine the average Galactic gas-to-dust ratios. The analysis is performed separately for both Galactic hemispheres mainly due to the presence of the Magellanic System (e.g. Nidever et al. 2010), which may affect the correlation results (Sect. 5).

3.3. Definition of MIVCs

The Gaussian decomposition of the GASS reveals that the Galactic atomic hydrogen is characterised by narrow and wide spectral lines that correspond to cold and warm gas (Kalberla & Haud 2015, their Fig. 1). The cold atomic component may be associated with molecular gas (e.g. Snow & McCall 2006). Accordingly, we define selection criteria for MIVCs that target cold H I gas with high line intensities.

These criteria are matching the observable properties of the well studied MIVCs IVC 135 (Weiß et al. 1999) and IVC 210 (Désert et al. 1990). Both objects have been extensively studied with the data from the Effelsberg 100 m telescope (Weiß et al. 1999; Lenz et al. 2015; Röhser et al. 2014). Both IVC 135 and IVC 210 have peak H I column densities of $N_{\rm H\,I}^{\rm peak} \simeq 2.5 - 3 \times 10^{20}\,{\rm cm^{-2}}$ and line width of the cold H I gas of FWHM $\simeq 4 - 5\,{\rm km\,s^{-1}}$. These objects are well known because they dominate the total gas and dust emission along their lines-of-sight. Hence, observationally an MIVC contains 1) sufficiently high IVC H I column density, 2) cold gas within the IVC velocity regime $20\,{\rm km\,s^{-1}} \leq |v_{\rm LSR}| \leq 100\,{\rm km\,s^{-1}}$, and 3) statistically significant H_2 column density. In addition, there is 4) only little LVC gas.

1. For IVC 135 and IVC 210 the transition from atomic to molecular hydrogen occurs at $N_{\rm H\,I}^0 = 1 - 2 \times 10^{20}\,{\rm cm^{-2}}$ (Weiß et al. 1999; Lenz et al. 2015; Röhser et al. 2014, 2016). We require the MIVC candidates to have $N_{\rm H\,I}^{\rm IVC} > 1 \times 10^{20}\,{\rm cm^{-2}}$.
2. Rapid H_2 formation is expected to be associated with cold and dense gas (e.g. Snow & McCall 2006). The H I line widths set upper limits on the kinetic temperature of the

Table 2: Fitted global linear parameters for the northern and southern Galactic hemispheres at latitudes of $|b| > 20°$. Details of the fitting procedure are given in the text. The statistical errors on the parameters are of the order of $\sim 10^{-4}$ in the given units.

north			south		
R	$\epsilon^{\rm LVC}$	$\epsilon^{\rm IVC}$	R	$\epsilon^{\rm LVC}$	$\epsilon^{\rm IVC}$
$[10^{-6}]$	$[10^{-26}\,{\rm cm}^2]$	$[10^{-26}\,{\rm cm}^2]$	$[10^{-6}]$	$[10^{-26}\,{\rm cm}^2]$	$[10^{-26}\,{\rm cm}^2]$
0.068	0.754	0.451	−0.148	0.723	0.637

gas. Observationally, MIVCs have Gaussian line components with amplitudes larger than $A_{\rm gauss} > 10\,{\rm K}$ and line widths of $FWHM_{\rm gauss} < 5\,{\rm km\,s^{-1}}$, corresponding to $T_{\rm kin} < 545\,{\rm K}$. This is a mild upper limit since the actual gas temperatures are significantly lower, as is inferred by CO observations (e.g. Heyer & Dame 2015). The line parameters are not extracted from the H I survey data directly but from a Gaussian decomposition (Sect. 2.1).

3. The intrinsic scatter of the H I-FIR correlation is used as a measure for the statistical significance of the derived H_2 column densities $N_{\rm H_2}$. Towards regions with $N_{\rm HI}^{\rm TOT} = N_{\rm HI}^{\rm LVC} + N_{\rm HI}^{\rm IVC} < 1 \times 10^{20}\,{\rm cm}^{-2}$ no H_2 is expected and the scatter of the H I-FIR correlation is assumed to be caused by intrinsic variations of the correlation. For these parts of the sky, we calculate from the derived H_2 map (Sect. 3.1) the median $\tilde{N}_{\rm H_2}$ and standard deviation $\sigma(N_{\rm H_2})$ across the hemispheres. This translates into 3σ criteria of $N_{\rm H_2} > \tilde{N}_{\rm H_2} + 3\sigma(N_{\rm H_2})$.
4. If the LVC H I column density towards IVC gas is large, molecules may be located within LVCs causing FIR excess emission that might be falsely associated with IVC gas. Furthermore, the imprint of the IVC on the H I-τ correlation may be marginal and, thus, FIR excess within the IVC gas may not be correctly identified. Hence, we require MIVC candidates to significantly contribute to the total H I column density along their lines-of-sight by choosing $N_{\rm HI}^{\rm LVC} < 2N_{\rm HI}^{\rm IVC}$.

More candidates can be obtained by relaxing either criterion. Our goal here is, however, to find all of the clear and distinct MIVC candidates.

We identify extended regions that fulfil these four criteria simultaneously. We do not require the candidates to have a minimum angular size since there may be only a few connected pixels that satisfy all criteria and exceed the required thresholds. Nevertheless, also these candidates are interesting objects since they may indicate the 'tip of the iceberg' of a potential MIVC. In the subsequent analysis we distinguish between objects that have angular extents that are larger or smaller than the resolution element of our study, which is a single GASS beam (Table 1).

In order to allow small angular offsets between the different observables ($N_{\rm HI}^{\rm IVC}$, $A_{\rm gauss}$, $FWHM_{\rm gauss}$, $N_{\rm H_2}^{\rm IVC}$, $N_{\rm HI}^{\rm LVC}$) we apply maximum filters with the size of the angular resolution of GASS. Small shifts between the different observables are likely to occur, e.g. due to the FIR emission of LVC gas.

Our search distinguishes between IVC gas at negative and positive LSR velocities with $-100\,{\rm km\,s^{-1}} \le v_{\rm LSR} \le -20\,{\rm km\,s^{-1}}$ or $+20\,{\rm km\,s^{-1}} \le v_{\rm LSR} \le +100\,{\rm km\,s^{-1}}$. In the following these two different regimes are denoted as MIVC$^{\pm}$.

3.4. Ranking of inferred MIVC candidates

There is a large number of inferred MIVC candidates, some of which are more reliable than others. We quantify the significance

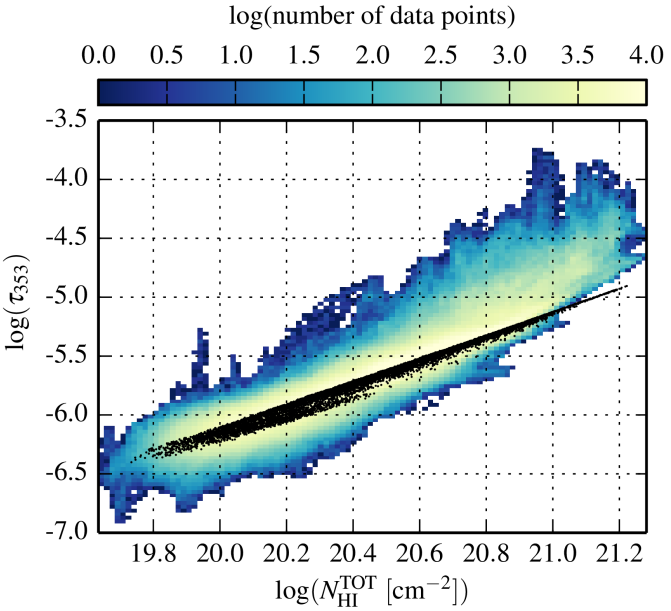

Fig. 1: H I-τ correlation plot for the northern Galactic hemisphere at $b > 20°$. The H I column density is the combined LVC and IVC emission between $-100\,{\rm km\,s^{-1}} \le v_{\rm LSR} \le +100\,{\rm km\,s^{-1}}$. The black dots show the two-component linear model consisting of LVC and IVC contributions. From this model 10000 data points are chosen randomly and plotted.

S of each candidate by

$$S = \frac{\epsilon_{cand}^{\rm IVC}}{\sigma\left(\epsilon_{cand}^{\rm IVC}\right)} \times \sqrt{N} \qquad (4)$$

where $\epsilon_{\rm cand}^{\rm IVC}$ is the estimated slope of the *local* H I-τ correlation in a small region of $2° \times 2°$ around the centre of each candidate. Moreover, $\sigma\left(\epsilon_{\rm cand}^{\rm IVC}\right)$ is the corresponding fitting uncertainty and N is the number of pixels of each candidate, enhancing larger regions that fulfil the criteria. The local H I-τ correlation is fitted the exact same way as the global H I-τ correlation (Sect. 3.2).

4. Northern Galactic hemisphere

In Fig. 1 we plot the resulting correlation for the northern Galactic hemisphere at $b > 20°$. The two component linear model is fitted and the resulting linear parameters are compiled in Table 2.

The data has a large scatter around the estimated linear model. Above $\log(N_{\rm HI}^{\rm TOT}/[{\rm cm}^{-2}]) \simeq 20.3$ the correlation steepens significantly, which is thought to reflect the presence of molecular hydrogen. Even at $b > 20°$ there are lines-of-sight exceeding $N_{\rm HI}^{\rm TOT} \simeq 10^{21}\,{\rm cm}^{-2}$, which indicate large amounts of molecular gas due to the large FIR excess. At such high H I col-

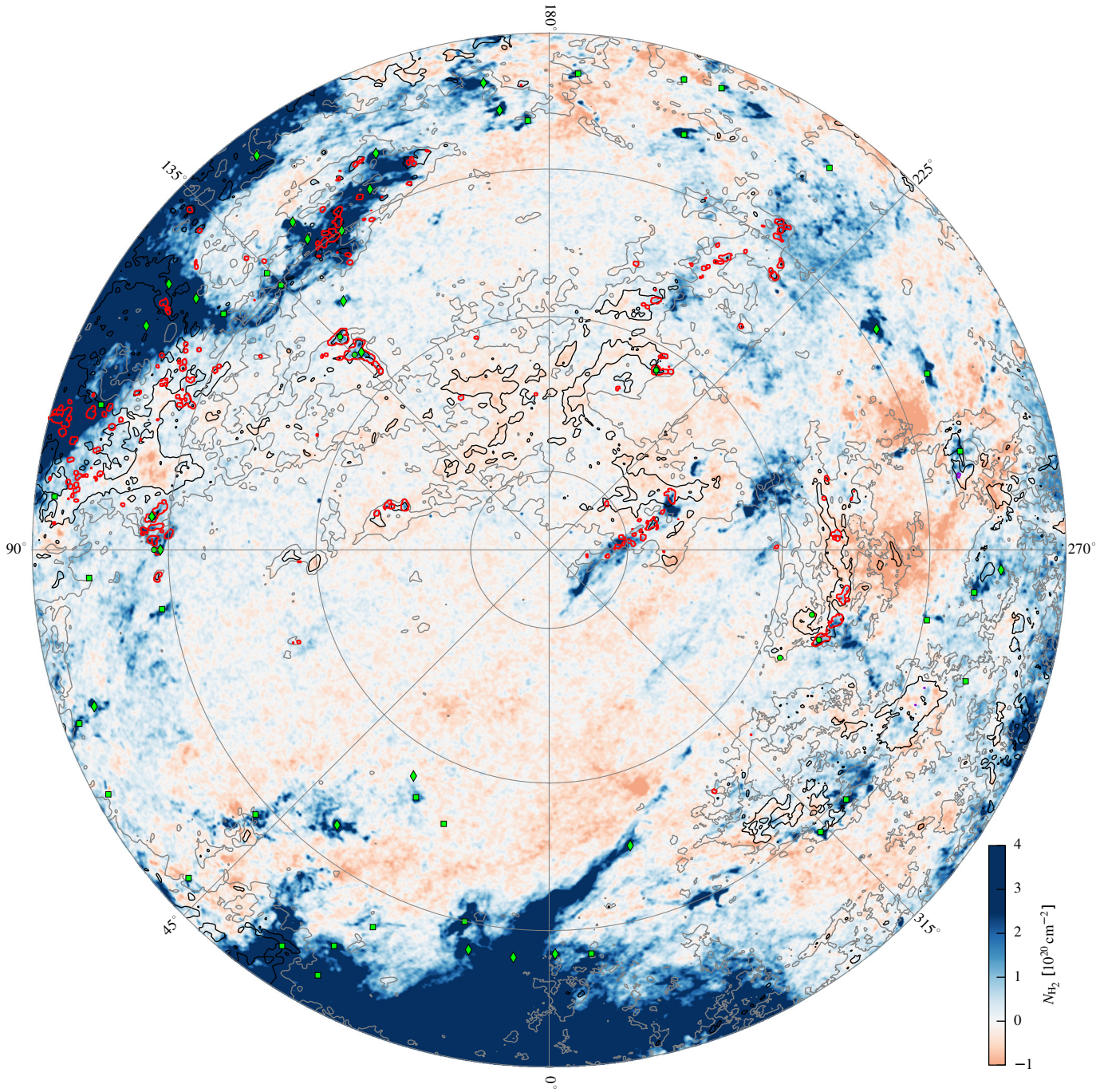

Fig. 2: Distribution of inferred H_2 column densities and MIVC$^{\pm}$ candidates for the northern Galactic hemisphere at $b > 20°$. The map is plotted in zenith-equal area projection centred on the northern Galactic pole with Galactic coordinates. The iso-latitude rings are placed at 20° with an increment of 20°. Blue and red colours indicate positive and negative N_{H_2}. The grey and black contours denote the total integrated (negative and positive) IVC H I gas at $N_{H\,I}^{IVC} = 0.75 \times 10^{20}$ cm^{-2} and 1.5×10^{20} cm^{-2} respectively tracing the location of IVC complexes. The red contours give the location of the inferred MIVC^{-} candidates, the dark-violet contours that of the MIVC^{+} candidates (Tables 5 and 6). The green circles mark the location of confirmed MIVCs as listed in Magnani & Smith (2010). The green diamonds indicate known high-latitude molecular clouds from FIR excess emission, the green squares give the positions of unidentified FIR excess sources as listed in Reach et al. (1998, their Tables 3 and 4).

umn densities H I absorption occurs (Strasser & Taylor 2004, their Fig. 10).

The best-fit linear parameters R, ϵ^{LVC}, and ϵ^{IVC} are inserted into Eq. (3) to calculate H_2 column densities across the northern Galactic hemisphere relative to the global average gas-to-dust ratios. The resulting H_2 distribution is shown in colour in Fig. 2 with the northern Galactic pole at the centre. The grey and black contours mark the total IVC H I column density at levels of 0.75 and 1.5×10^{20} cm^{-2}. Known high-latitude molecular clouds are marked by the green diamonds (Reach et al. 1998, their Table 3), additional FIR-excess clouds identified by Reach et al. (1998,

their Table 4) as the green squares. The green circles show the positions of confirmed MIVCs (Magnani & Smith 2010).

The new H I and FIR data allows to study the FIR excess emission on much smaller angular scales revealing many additional excess objects. Note that the H_2 map presented in Fig. 2 is quantitatively only valid for the IVC gas.

Generally, the IVC gas appears to be FIR deficient relative to the Galactic average. This is expected because of two reasons. Firstly, IVCs typically have metallicites slightly lower than solar (e.g. Wakker 2001) resulting in potentially lower amounts of dust. Secondly, IVCs are located at distances of up to ~2 kpc (e.g. Wakker 2001), reducing the strength of the radiation field by which the dust is heated.

4.1. The northern Galactic MIVC population

At total H I column densities of less than $N_{\rm H\,I}^{\rm TOT} \leq 1 \times 10^{20}\,{\rm cm}^{-2}$, we infer a median of $\tilde{N}_{\rm H_2} \simeq 0.05{\times}10^{20}\,{\rm cm}^{-2}$ and a standard deviation of $\sigma(N_{\rm H_2}) \simeq 0.20{\times}10^{20}\,{\rm cm}^{-2}$. These quantities measure the intrinsic scatter and bias of the fitted northern H I-τ correlation. At $N_{\rm H\,I}^{\rm TOT} < 1 \times 10^{20}\,{\rm cm}^{-2}$ there is no significant amount of H_2 expected, which is consistent with our data. The median value is significantly less than the scatter. Hence, at 3σ significance a northern MIVC candidates requires $N_{\rm H_2}^{\rm IVC} = \tilde{N}_{\rm H_2} + 3\sigma(N_{\rm H_2}) \gtrsim 0.65 \times 10^{20}\,{\rm cm}^{-2}$.

Applying the four criteria for MIVCs results into candidates that are marked in Fig. 2 by the red and dark-violet contours for the MIVC$^-$ and MIVC$^+$ candidates, respectively. There is a very significant discrepancy in candidate numbers for the two velocity regimes towards the northern sky: Only three MIVC$^+$ candidates are detected as compared to 184 MIVC$^-$ candidates. 134 of the MIVC$^-$ candidates exceed the size of a single GASS beam (Table 5), 50 are smaller (Table 6). Only a single MIVC$^+$ candidate is larger (Table 5), two are smaller than the GASS beam (Table 6).

All previously known MIVCs (Magnani & Smith 2010) are identified as candidates. Only G 295.0+57.1 is not recovered because it is not well separated by the LSR velocity limit at $v_{\rm LSR} = -20\,{\rm km\,s}^{-1}$. Still, there is FIR excess emission associated with this object. These results confirm our definition of MIVCs (Sect. 3.3) and justifies the simplifications made in the global H I-τ correlation. The complete sample of MIVC$^\pm$ candidates is compiled in Tables 5 and 6.

The MIVCs$^-$ are located mostly towards the outer Galactic disk at mean latitudes of $\bar{b} \simeq 45^\circ$ and the MIVC$^+$ candidates at $\bar{b} \simeq 35^\circ$, which is well above the limit of $b = 20^\circ$. The candidates are not isolated and often part of larger coherent IVC structures, like for instance Draco.

4.2. Comparison of northern MIVC candidate sample with kinematical model

The kinematics of the MIVC samples are compared to a model of Galactic rotation. For this we calculate the expected observable radial velocity for given coordinates l and b and Galactocentric radius R assuming the model of Galactic rotation $\theta(R)$ as parametrised by Brand & Blitz (1993, their Eq. 6). In this model the rotational velocity of the Sun is set to $\theta_0 = 220\,{\rm km\,s}^{-1}$ and its Galactocentric distance to $R_0 = 8.5$ kpc.

We include the additional radial and vertical velocity components $v_{\rm r} = -30^{+7}_{-5}\,{\rm km\,s}^{-1}$ and $v_{\rm z} = -20^{+5}_{-7}\,{\rm km\,s}^{-1}$ of the Galactic halo derived by Marasco & Fraternali (2011). Marasco & Fraternali (2011) estimate a vertical scale height of the extra-planar gas of $h_z = 1.6^{+0.6}_{-0.4}$ kpc with a rotational vertical lagging of $-15 \pm 4\,{\rm km\,s}^{-1}\,{\rm kpc}^{-1}$, i.e. the rotational velocity decreases away from the disk. These vertical and radial velocity components are projected onto the lines-of-sight for l and b by applying Eq. 3 of Marasco & Fraternali (2011) and converting the obtained LSR velocities into the Galactic standard of rest (GSR).

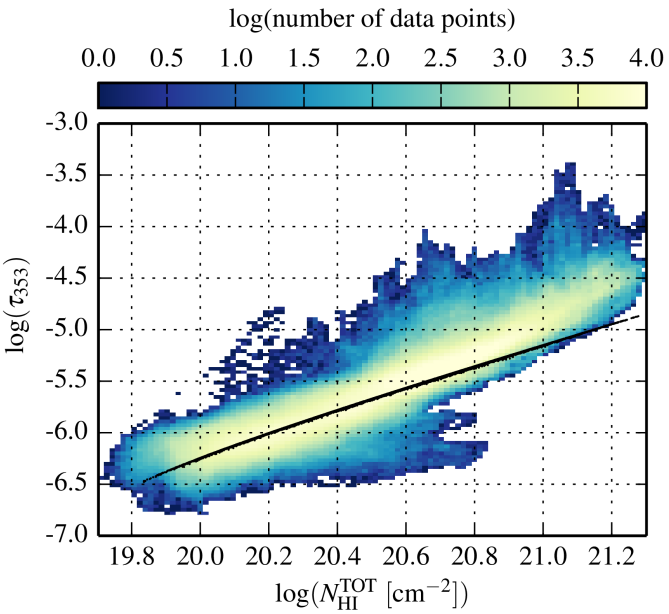

Fig. 4: H I-τ correlation plot for the southern Galactic hemisphere at $b < -20^\circ$. The H I column density is the combined LVC and IVC emission between $-100\,{\rm km\,s}^{-1} \leq v_{\rm LSR} \leq +100\,{\rm km\,s}^{-1}$. The black dots show the two-component linear model consisting of LVC and IVC contributions. From this model 10000 data points are chosen randomly and plotted.

For the projection of the radial velocity component, one has to assume some height above or below the disk, for which we take $z = 1.6$ kpc as estimated by Marasco & Fraternali (2011). The vertical lagging of $-15 \pm 4\,{\rm km\,s}^{-1}\,{\rm kpc}^{-1}$ is included in the rotational velocity $\theta(R, z)$. The parametrisation of the model is changed such that it is dependent on l, b, and the heliocentric distance d instead. The conversion between helio- and Galactocentric distance is calculated by applying Eq. 2 from Brand & Blitz (1993). Hence, we calculate the expected radial GSR velocity from Galactic rotation, modified by vertical, radial, and lagging velocity components. Note that d quantifies the heliocentric distance within the 2D plane of the Milky Way disk $z = 0$.

The resulting distribution of l-$v_{\rm GSR}$ is plotted for the northern Galactic hemisphere in Fig. 3 (top). The plots on the left- and right-hand side in this Figure are for the MIVC$^-$ and MIVC$^+$ samples, respectively. The data points represent the cloud parameters, while the different lines show the modelled rotation curve for different latitudes b (solid for 20°, dashed for 50°, dotted for 80°) and heliocentric distances d (red for 1 kpc, blue for 2 kpc, magenta for 3 kpc, black for 4 kpc, cyan for 5 kpc, respectively). The colours of the data points indicate the absolute value of the latitude coordinate of the candidates as shown by the colourbar.

Apparently, the distribution of the MIVC$^\pm$ candidates is well reproduced by the rotational model of Marasco & Fraternali (2011), either by changing Galactic latitudes or heliocentric distances. This is an argument favouring the origin of IVCs from Galactic fountains.

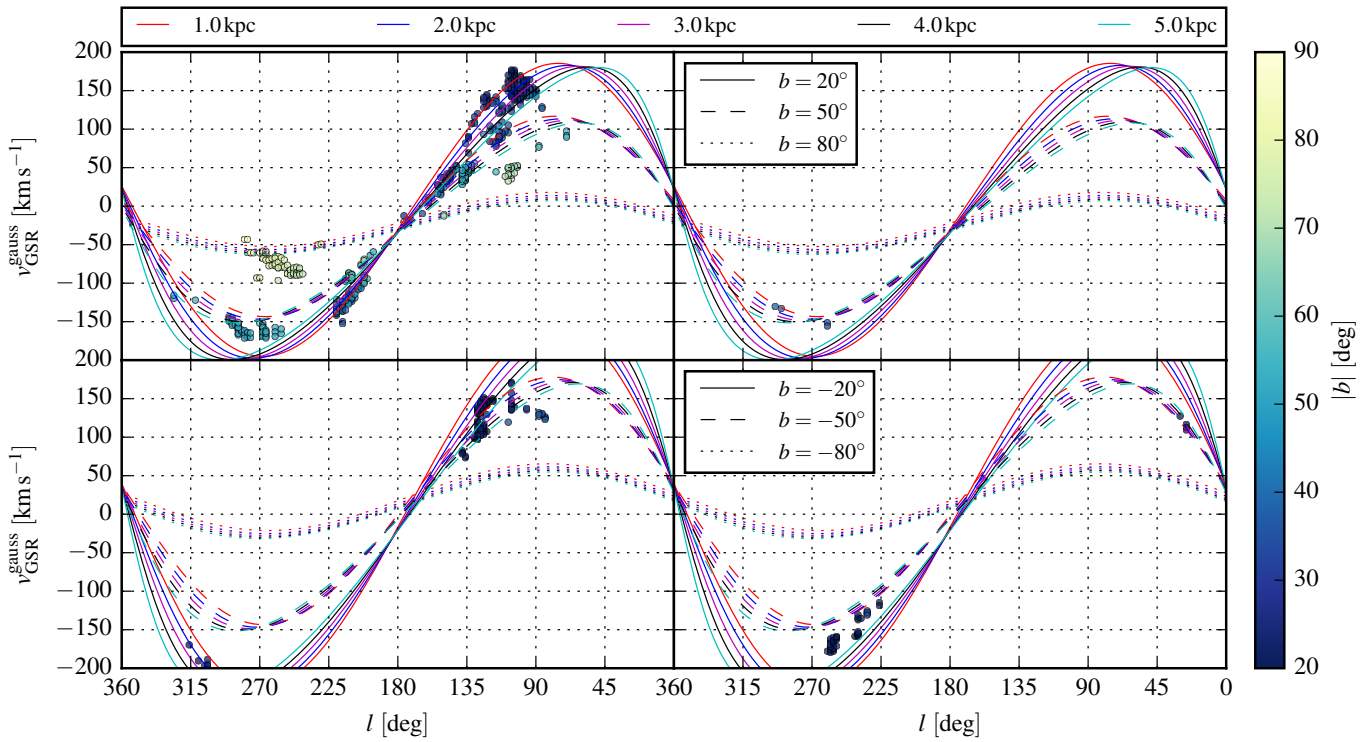

Fig. 3: Radial GSR velocities of northern (*top*) and southern (*bottom*) MIVC$^{\pm}$ samples compared with Galactic longitudes l, left for the MIVCs^{-}, right for the MIVCs^{+}. The velocities of the individual candidates are given by the $v_{\rm GSR}^{\rm gauss}$ from the Gaussian decomposition of the H I survey data. The colour of each point encodes the absolute value of the latitude coordinate b of the candidates as indicated by the colorbar. The different lines show the modelled rotation velocities including a radial, vertical, and lagging velocity component as estimated by Marasco & Fraternali (2011). Their vertical height $z = 1.6$ kpc is assumed, for which the velocities are modelled at some heliocentric distances d and latitudes b as given in the legends. The solid, dashed, and dotted lines are for $b = 20°$, $b = 50°$, and $b = 80°$. The red, blue, magenta, black, and cyan lines are for heliocentric distances within the Galactic plane of $d = 1$ kpc, 2 kpc, 3 kpc, 4 kpc, and 5 kpc.

5. Southern Galactic hemisphere

As for the northern Galactic hemisphere (Sect. 4), the same correlation and fitting is performed for the southern hemisphere at $b < -20°$, except for the the Magellanic System. The Magellanic System covers a large fraction of the southern Galactic hemisphere stretching over the entire LVC and IVC velocity ranges, but it is not detected in FIR emission (e.g. Planck Collaboration XXIV 2011; Brüns et al. 2005). Hence, the Magellanic System is expected to behave differently in terms of the H I-τ correlation than the Milky Way gas, which may introduce systematic biases in the fitting of the Galactic H I-τ correlation. Thus, we exclude the Magellanic System when fitting the H I-τ correlation. Otherwise, the Magellanic System is included in the analysis, since we cannot be sure that we mask the emission correctly.

For this masking the 3D H I model of the Milky Way from Kalberla & Dedes (2008) is applied in order to separate the H I emission into Galactic and Magellanic H I gas. We use the same clipping values as Planck Collaboration XVII (2014) who attribute H I emission to the Magellanic System if the modelled Milky Way H I emission is $T_{\rm B}^{\rm model} \leq 60$ mK. This corresponds to a deviation velocity (Wakker 1991) of $v_{\rm dev} \simeq 45$ km s^{-1}.

The masking of the Magellanic System impacts the estimated offset and IVC slope by a few percent. While the LVC dust emissivity $\epsilon^{\rm LVC}$ is comparable for both Galactic hemispheres, the IVC dust emissivity $\epsilon^{\rm IVC}$ is significantly larger on the southern Galactic hemisphere. The H I-τ correlation plot is shown in Fig. 4. As for the northern, the correlation widens at $\log N_{\rm H\,I}^{\rm TOT}/[{\rm cm}^{-2}] \simeq 20.4$ suggesting the presence of H_2 and the unusual correlation properties of the Magellanic System, which appears as very FIR dim material with $\tau \lesssim 10^{-6}$. The inferred model does not produce such a large scatter as for the northern Galactic hemisphere, which reflects the dominance of the LVC gas over the IVC gas in terms of the FIR emission.

Note that the identical fitting method is applied, except for the masking of the Magellanic System. We attribute this different slope to the lack of extended high-latitude IVC gas with faint FIR emission. Instead, most of the IVC gas, as indicated by the grey and black contours, is located at lower absolute latitudes of $b > -40°$ (Fig. 5), which may lead to biases of the IVC slope by the LVC material. Furthermore, the estimated offset on the southern hemisphere is negative, which is an unphysical fitting result. Potential reasons for this are discussed in Sect. 7.4.

As for the northern Galactic hemisphere, the resulting H_2 distribution is plotted in Fig. 5. Towards the southern Galactic pole there is some IVC gas, which appears to be substantially FIR deficient with respect to the Galactic average. This material is likely part of the Magellanic Stream (Planck Collaboration XVII 2014).

5.1. The southern Galactic MIVC population

From the computed H_2 column densities at $N_{\rm H\,I}^{\rm TOT} < 1 \times 10^{20}$ cm^{-2}, we calculate a median $\tilde{N}_{\rm H_2} \simeq 0.13 \times 10^{20}$ cm^{-2}

and a standard deviation $\sigma(N_{\rm H_2}) \simeq 0.15 \times 10^{20}\,{\rm cm^{-2}}$. Hence, a southern Galactic MIVC candidate requires $\tilde{N}_{\rm H_2} + 3\sigma(N_{\rm H_2}) \simeq 0.58 \times 10^{20}\,{\rm cm^{-2}}$ to be identified. As compared to the northern hemisphere, the offset is larger but the scatter is smaller. This reflects the smaller amount of IVC gas on the southern hemisphere.

We apply the four criteria for MIVCs and plot the identified MIVC$^-$ candidates as the red and the MIVC$^+$ candidates as the dark-violet contours in Fig. 5. There are 31 MIVC$^-$ and 21 MIVC$^+$ candidates on the southern Galactic hemisphere. The 19 MIVC$^-$ candidates that are larger than the GASS beam are compiled in Table 5, the 12 that are smaller in Table 6. For the MIVC$^+$ candidates, 17 are larger (Table 5) and four are smaller than the beam (Table 6). The MIVC$^-$ candidates are located at low absolute latitudes of $\bar{b} \simeq -23°$, the MIVC$^+$ candidates at $\bar{b} \simeq -22°$, both are located close to the latitude limit of $b = -20°$.

5.2. Comparison of southern MIVC candidate sample with kinematical model

The same rotational model as for the northern Galactic hemisphere (Sect. 4.2) is compared to the MIVC$^\pm$ candidate populations on the southern Galactic hemisphere. The resulting plots (Fig. 3, bottom) show that apparently the MIVC$^\pm$ samples are consistent with the modified Galactic rotation model.

6. Results

6.1. Physical properties of MIVC candidates

Here, we estimate some basic physical properties of the northern and southern MIVC candidate ensembles. We are especially interested in the pressure and mass within these objects. For the candidates that have an angular extent smaller than the GASS beam, we calculate the respective parameters for all pixels within the beam solid angle. We explicitly distinguish between the parameters for objects that are larger or smaller than the beam.

6.1.1. Derivation

The pressure p of an H I gas is calculated from the observables H I particle density $n_{\rm H\,I}$ and kinetic gas temperature $T_{\rm kin}$ by

$$\frac{p}{k_{\rm B}} = n_{\rm H\,I} T_{\rm kin} \tag{5}$$

in units of the Boltzmann constant $k_{\rm B}$.

Assuming spherical symmetry, the H I particle density of an individual candidate is inferred from its peak H I column density and its spatial extent d by

$$n = \frac{N_{\rm H\,I}}{d}. \tag{6}$$

The spatial extent d depends on the unknown distance D. The candidate clouds are likely located within the disk-halo interface of our Galaxy, embedded in a thin and diffuse H I layer (e.g. Kalberla & Kerp 2009). This layer also contributes to the measured H I column density of the candidate cloud but its contribution is unrelated to the object. In order to quantify this additional contribution, we take the median H I column density within 5° around the candidate and subtract this background column density from its peak H I column density.

The angular extent of each candidate is converted into the angular diameter α of a sphere. The actual spatial size d of a candidate depends on the distance D to the cloud by $d = \alpha D$. However, the distance is generally unknown for most candidates. As discussed in Sect. 6.1.2 we adopt vertical distributions for the candidate samples from which the distance D to each object is calculated.

The kinetic temperature of the H I gas is obtained from the decomposition of HI lines into Gaussian components. The observed and modelled line widths Δv are upper limits to the kinetic gas temperature (e.g. Kalberla & Kerp 2009):

$$T_{\rm kin} \leq \frac{m_{\rm H}}{8\,k_{\rm B}\,\ln 2}\,(\Delta v)^2 \simeq 21.8\,{\rm K}\left(\frac{\Delta v}{[{\rm km\,s^{-1}}]}\right)^2 \tag{7}$$

with the mass of an hydrogen atom $m_{\rm H}$.

The H I mass $M_{\rm H\,I}$ of a candidate cloud is the integral of the H I column densities across the angular extent Ω of the object:

$$M_{\rm H\,I} = m_{\rm H} D^2 \int_{\rm source} {\rm d}\Omega\, N_{\rm H\,I}(l,b). \tag{8}$$

The total hydrogen mass $M_{\rm H}$ of a candidate cloud is the sum of the H I mass $M_{\rm H\,I}$ and the mass in molecular hydrogen $M_{\rm H_2}$. $M_{\rm H_2}$ is computed like Eq. (8) for the H_2 column densities $N_{\rm H_2}(l,b)$ but with an additional factor of two.

The molecular fraction $f_{\rm mol}$ of a candidate MIVC is given by

$$f_{\rm mol} = \frac{2N_{\rm H_2}}{N_{\rm H\,I} + 2N_{\rm H_2}} = \frac{M_{\rm H_2}}{M_{\rm H\,I} + M_{\rm H_2}}. \tag{9}$$

6.1.2. Distances to the IVC gas

For the well studied MIVCs there are good distance constraints of 300 − 400 pc (Gladders et al. 1998; Benjamin et al. 1996; Röhser et al. 2014). However, for the majority of IVC gas there are no distance constraints except for the global upper limits of ∼2 kpc (e.g. Wakker 2001). In order to obtain a rough distance estimate to the bulk IVC gas, we assume that the IVCs are caused by a Galactic fountain process.

A Galactic fountain lifts material in the lower halo to some height z described by some vertical distribution (e.g. Bregman 1980). We assume that the IVC gas is distributed according to a sech^2 profile (Marasco & Fraternali 2011) with vertical scale heights of $h_z = 0.5$ kpc and $h_z = 1.6$ kpc. The latter height is derived by Marasco & Fraternali (2011) for the Milky Way halo. From the height z, the corresponding distance D is then given by $D = z/\sin|b|$.

Since this approach focuses on the statistical properties of the MIVC candidate samples, we calculate the parameters for 1000 different realisations of the vertical distribution. The given numbers are the median values from all realisations.

6.1.3. Results

In Table 3 we give the median of the inferred physical properties of each IVC population (northern MIVCs$^\pm$, southern MIVCs$^\pm$). Furthermore, we distinguish between samples with angular sizes Ω larger or smaller than the GASS beam $\Omega_{\rm GASS}$. For the largest sample, the northern MIVCs$^-$, we additionally show histograms of the spatial sizes d, kinetic temperatures $T_{\rm kin}$, H I particle densities $n_{\rm H\,I}$, and pressures $p/k_{\rm B}$, separately for objects larger and smaller than the beam (Fig. 6, top and bottom). Note that there are only three northern MIVC$^+$ candidates.

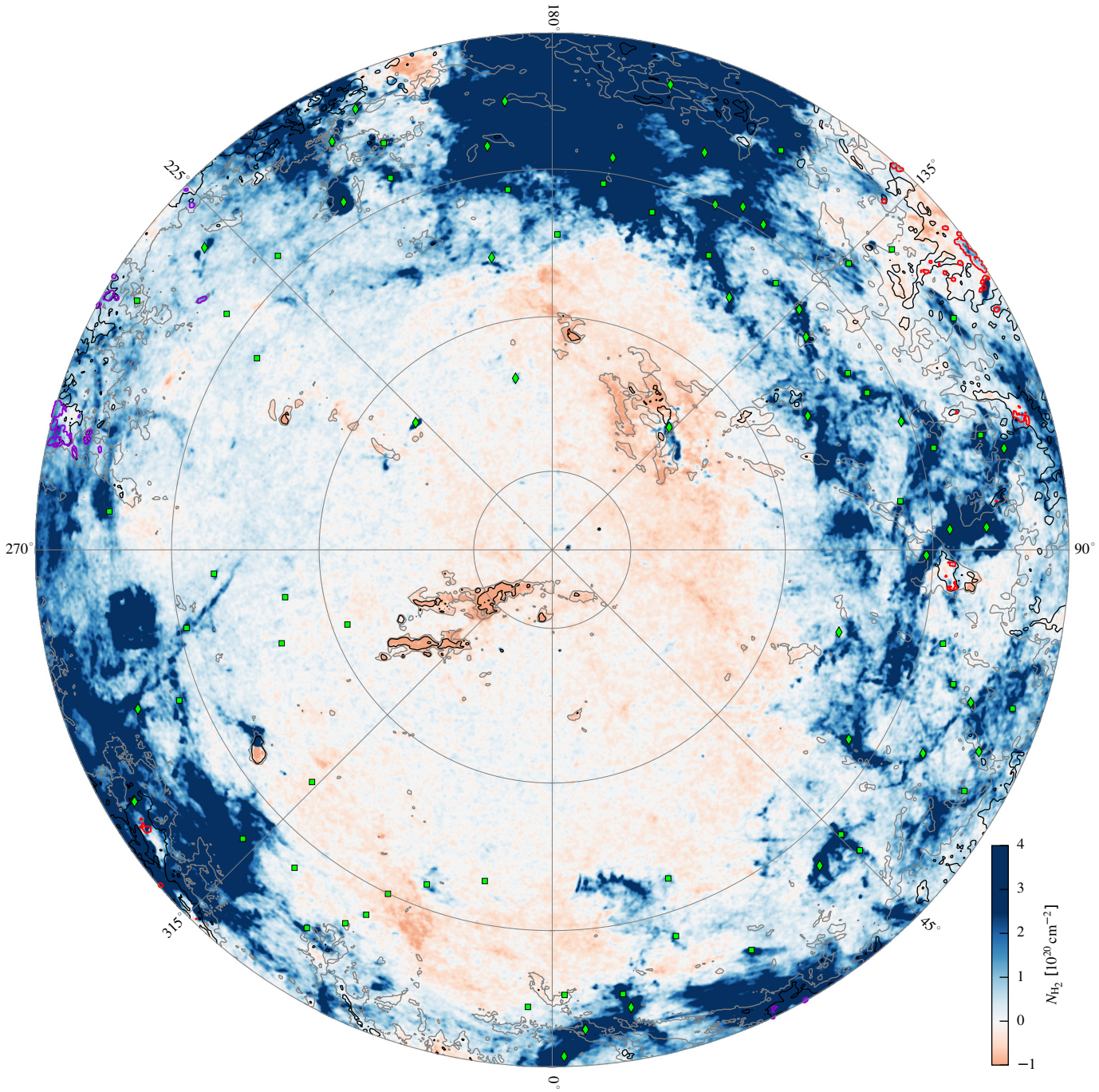

Fig. 5: Distribution of southern MIVC$^{\pm}$ candidates at $b < -20°$ on top of the inferred H_2 column densities. The map is plotted in zenith-equal area projection centred on the southern Galactic pole with Galactic coordinates. The iso-latitude rings are placed at $-20°$ with a decrement of $-20°$. All blue colours indicate positive N_{H_2}, all red negative N_{H_2}. The grey and black contours denote the total integrated (negative and positive) IVC H I gas at $N_{H\,I}^{IVC} = 0.75 \times 10^{20}$ cm^{-2} and 1.5×10^{20} cm^{-2} respectively tracing the location of IVC complexes. The red and dark-violet contours give the location of the inferred MIVC^{-} and MIVC^{+} candidates (Tables 5 and 6). The green diamonds indicate known high-latitude molecular clouds from FIR excess emission, the green squares give the positions of unidentified FIR excess sources as listed in Reach et al. (1998, their Tables 3 and 4).

– The median angular diameters of the MIVC candidates are below ∼37′. This is about or below the angular resolution of the LAB survey (Kalberla et al. 2005) that has been used in previous studies of the H I-τ correlation. Hence, these studies did not resolve the candidates spatially, rendering the candidates potentially undetectable.

– The median upper limits of the kinetic temperatures are $T_{kin} \lesssim 500$ K, which is typical for the CNM (e.g. Kalberla & Kerp 2009). The corresponding line widths are FWHM $\lesssim 4.8$ km s^{-1}, close to the applied upper line width criterion for the definition of MIVCs of FWHM ≤ 5 km s^{-1}. Hence, we may have excluded some objects due to this selection.

Table 3: Median values of estimated angular extents θ, spatial extents d, kinetic temperatures $T_{\rm kin}$, densities $n_{\rm H\,I}$, pressures $p/k_{\rm B}$, molecular fractions $f_{\rm mol}$, H I masses $M_{\rm H\,I}$, H_2 masses $M_{\rm H_2}$, and total hydrogen masses $M_{\rm H}$ of northern and southern MIVC$^{\pm}$ samples. The samples are subdivided between angular sizes Ω larger or smaller than the GASS beam $\Omega_{\rm GASS}$. The quantities are computed for distances that are obtained from 1000 realisations of vertical distributions with scale heights of $h_z = 0.5$ kpc and $h_z = 1.6$ kpc, from which the distances to the candidates are calculated for their latitudes b (Sect. 6.1.2). Note that there is only one northern MIVC^{+} candidate with $\Omega > \Omega_{\rm GASS}$.

	θ [arcmin]	d [pc]	$T_{\rm kin}$ [K]	$n_{\rm H\,I}$ [cm^{-3}]	$p/k_{\rm B}$ [K cm^{-3}]	$f_{\rm mol}$	$M_{\rm H\,I}$ [M$_\odot$]	$M_{\rm H_2}$ [M$_\odot$]	$M_{\rm H}$ [M$_\odot$]
$\Omega \geq \Omega_{\rm GASS}$									
northern MIVCs^{-}	33.4	8.8/28.7	411	3.9/1.2	1560/500	0.55	75/760	90/990	210/2280
southern MIVCs^{-}	31.4	13.6/42.8	437	5.2/1.8	2160/730	0.37	310/2480	140/1380	580/5560
northern MIVCs^{+}	23.8	6.9/20.0	472	14.3/4.9	6730/2310	0.28	90/750	35/290	120/1040
southern MIVCs^{+}	36.6	14.7/46.0	386	2.8/0.9	920/290	0.54	210/2100	300/3320	510/5280
$\Omega < \Omega_{\rm GASS}$									
northern MIVCs^{-}	10.8	2.5/7.8	427	10.4/3.1	3840/1150	0.41	4.1/44	3.9/42	8.1/86
southern MIVCs^{-}	9.4	3.1/10.6	482	15.5/4.8	7140/2160	0.28	15/130	7.7/80	25/240
northern MIVCs^{+}	5.2	1.4/4.5	441	43.9/13.3	19400/5960	0.23	2.7/29	0.8/8.9	3.5/37.9
southern MIVCs^{+}	10.7	4.4/13.8	510	16.1/5.0	7890/2500	0.34	25/240	8.0/80	30/310

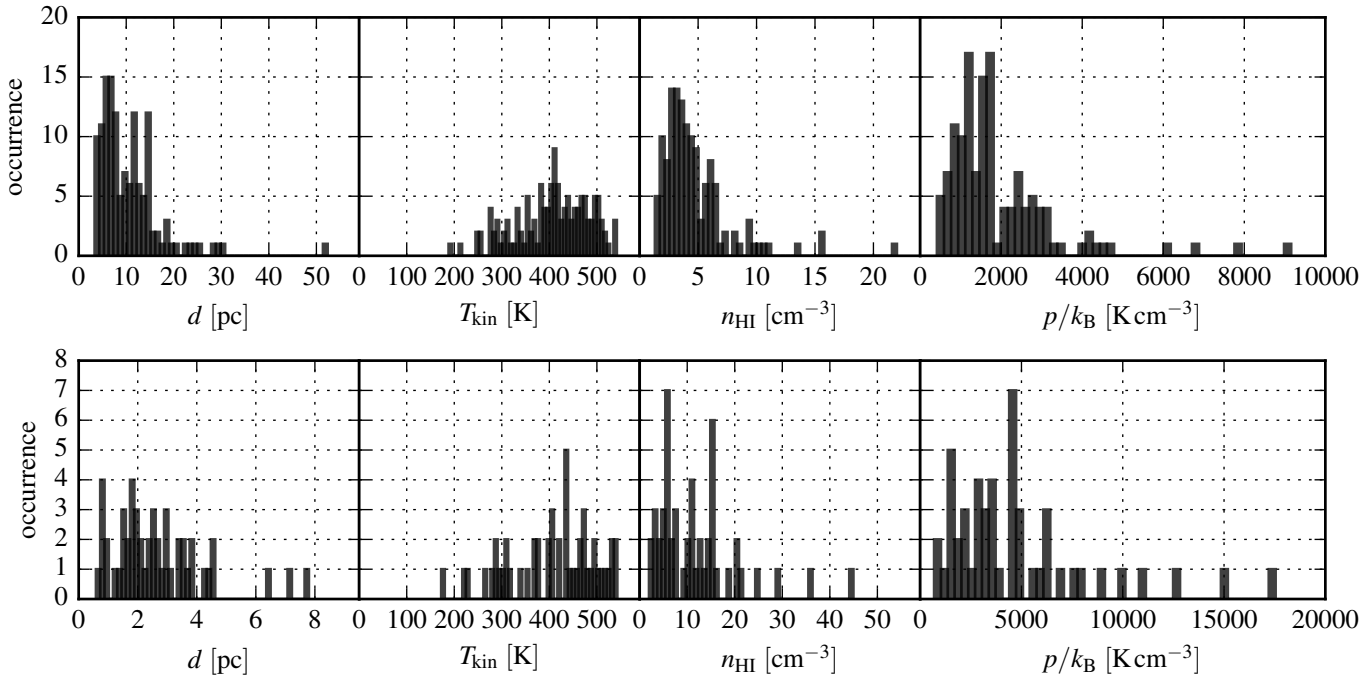

Fig. 6: Spatial sizes d, kinetic temperatures $T_{\rm kin}$, H I particle densities $n_{\rm H\,I}$, and pressures $p/k_{\rm B}$ of northern MIVC^{-} ensemble. All objects with angular sizes exceeding the GASS beam are shown on the top, all objects smaller that are smaller on the bottom. The properties are the median values derived from 1000 realisations of the vertical distribution with a scale height of $h_z = 0.5$ kpc (Sect. 6.1.2).

– The median H I particle densities are $n_{\rm H\,I} \simeq 1 - 40\,{\rm cm^{-3}}$, typical for the CNM (e.g. Kalberla & Kerp 2009).

– The median pressure is $p/k_{\rm B} = 300 - 8000\,{\rm K\,cm^{-3}}$. For the largest sample, the northern MIVCs^{-}, the median pressure within the atomic gas is $\sim$1560 K cm^{-3}, which is less than the average equilibrium thermal pressure in the ISM of $\sim$3000 K cm^{-3} (e.g. Wolfire et al. 2003). Many MIVC candidates appear to be over-pressured relative to the surrounding medium when the pressure contribution from H_2 and the decreasing equilibrium thermal pressure with scale height (Wolfire et al. 1995) is considered.

– The median molecular fractions are high with $f_{\rm mol} \simeq 0.2 - 0.6$, typical for diffuse and translucent molecular clouds (Snow & McCall 2006).

The candidates that are smaller than the GASS beam tend to have higher Doppler temperatures than those that are more extended. In combination with their higher densities the pressures are larger.

This may indicate unresolved velocity and angular structure within the less extended candidates. This is consistent with the results of Röhser et al. (2016) obtained from high-resolution HI and CO observations of high-latitude IVCs. For the MIVC IVC 210 they estimate densities of up to 500 cm^{-3} from ^{12}CO(1 $\rightarrow$ 0) measurements. Hence, the derived parame-

ters (Table 3) are certainly only upper limits for spatial extents or gas temperatures and lower limits for particle density or molecular fraction.

Furthermore, the molecular fractions of the small objects tend to be lower. This may be related to the fact that molecules form in compact unresolved structures. Our estimates are averages, which may reduce the molecular fraction systematically.

6.1.4. Mass estimates

The total H I and H_2 mass in all potential MIVC candidates is estimated from vertical sech^2 distributions with vertical scale heights of $h_z = 0.5$ kpc and $h_z = 1.6$ kpc for all IVCs. The latter is the height derived by Marasco & Fraternali (2011). Furthermore, all negative H_2 column densities are discarded (compare with Figs. 2 and 5). Again, we distinguish between objects larger or smaller than the beam.

The molecular mass constitutes a significant fraction of the total gaseous mass of the MIVC candidates (Table 4). Figures 2 and 5 reveal that potential MIVCs represent only a small fraction of all IVCs. In addition, Marasco & Fraternali (2011) find an HI mass of the Milky Way halo of $3.2^{+1.0}_{-0.9} \times 10^8\,\mathrm{M}_\odot$, which is significantly larger than the derived masses here. Hence, molecular hydrogen is only a small fraction of the total gaseous mass in Galactic IVCs. This is in line with the generally low number of confirmed MIVCs and the low H_2 column densities in many IVCs (Richter et al. 2003; Wakker 2006).

According to Marasco & Fraternali (2011) the upper inflow velocity of the halo material is $v_\mathrm{in} \simeq -50\,\mathrm{km s^{-1}}$. This results into upper limits on the H_2 inflow rate of the MIVC candidates of $\dot{M}_{\mathrm{H_2}} \simeq 0.006\,\mathrm{M_\odot\,yr^{-1}}$ to $0.02\,\mathrm{M_\odot\,yr^{-1}}$ for $h_z = 0.5$ kpc and $h_z = 1.6$ kpc. Together with the atomic mass in MIVC candidates, the inflow rate is between $\dot{M}_\mathrm{H} \simeq 0.009\,\mathrm{M_\odot\,yr^{-1}}$ and $0.03\,\mathrm{M_\odot\,yr^{-1}}$.

In terms of H I column density, about 2% of the northern IVC gas with negative LSR velocity is associated with MIVC candidates. Using this simple extrapolating factor for the atomic gas and assuming that the H_2 mass is negligible in the other IVC gas, the inflow from the total northern atomic and molecular IVC gas is $\sim 0.16\,\mathrm{M_\odot\,yr^{-1}}$ to $0.52\,\mathrm{M_\odot\,yr^{-1}}$, which is similar to the inflow rates from Galactic HVCs (Putman et al. 2012). The estimated inflow from IVCs may contain a significant fraction of cooled halo material (Marinacci et al. 2010; Marasco et al. 2012). This combined IVC and HVC inflow rate appears to be below the Galactic star formation rate of $1.9 \pm 0.4\,\mathrm{M_\odot\,yr^{-1}}$ (Chomiuk & Povich 2011).

7. Discussion

In this paper we search for potential MIVC candidates of the Milky Way towards high Galactic latitudes. All previously known MIVCs are recovered except for a single one. This positive result justifies the simplifying assumptions in the inference of MIVCs. For instance we only consider a single gas-to-dust ratio for either northern or southern hemisphere. The fact that we still recover all the known MIVCs suggests that we capture their observational properties well. Also the local conditions appear not to change substantially across the sky.

The complete candidate list is given in Tables 5 and 6. These objects are ranked by analysing their *local* H I-τ correlation. Only Draco and IVC 135 are clearly associated with nearby HVC H I emission, for which this connection has been invoked explicitly as a possible formation channel (Herbstmeier et al. 1993; Moritz et al. 1998; Weiß et al. 1999; Lenz et al. 2015).

Table 4: Ensemble masses of $\mathrm{MIVC}^\pm$ samples on northern and southern Galactic hemispheres. The values are separately calculated for objects larger or smaller than one GASS beam. The masses are median values derived from 1000 realisations of the vertical distribution with a scale height of $h_z = 0.5$ kpc (Sect. 6.1.2). The masses for $h_z = 1.6$ kpc (Marasco & Fraternali 2011) are about ten times larger. Only positive H_2 column densities are considered.

	$M_{\mathrm{H\,I}}$ [$\mathrm{M_\odot}$]	$M_{\mathrm{H_2}}$ [$\mathrm{M_\odot}$]	M_H [$\mathrm{M_\odot}$]	$M_{\mathrm{H\,I}}$ [$\mathrm{M_\odot}$]	$M_{\mathrm{H_2}}$ [$\mathrm{M_\odot}$]	M_H [$\mathrm{M_\odot}$]
	$\Omega \geq \Omega_{\mathrm{GASS}}$			$\Omega < \Omega_{\mathrm{GASS}}$		
	$\mathrm{MIVC^-}$ samples					
north	$7.0{\cdot}10^4$	$1.8{\cdot}10^5$	$2.5{\cdot}10^5$	$1.2{\cdot}10^3$	$1.4{\cdot}10^3$	$2.6{\cdot}10^3$
south	$3.6{\cdot}10^4$	$3.0{\cdot}10^4$	$6.6{\cdot}10^4$	$5.7{\cdot}10^2$	$2.8{\cdot}10^2$	$8.5{\cdot}10^2$
	$\mathrm{MIVC^+}$ samples					
north	$8.8{\cdot}10^1$	$3.5{\cdot}10^1$	$1.2{\cdot}10^2$	$9.0{\cdot}10^0$	$3.0{\cdot}10^0$	$1.1{\cdot}10^1$
south	$2.6{\cdot}10^4$	$3.1{\cdot}10^4$	$5.7{\cdot}10^4$	$2.4{\cdot}10^2$	$3.8{\cdot}10^2$	$6.6{\cdot}10^2$

In all other cases this association is not observed. Hence, collisions between IVCs and HVCs appear not to be an important formation channel of MIVCs.

The detection of ^{12}CO(1→0) emission that is associated with the MIVC candidates is thought to be a definite prove of the molecular nature of the IVCs. However, the existence of CO-dark H_2 gas (Grenier et al. 2005; Wolfire et al. 2010; Planck Collaboration XIX 2011) indicates that there is a stage in the transition from atomic to molecular clouds that is not yet traceable by detectable amounts of CO emission (also Meyerdierks & Heithausen 1996; Duarte-Cabral & Dobbs 2016). For this molecular component the H I-FIR correlation is one of the few methods to identify and quantify this material.

7.1. Selection parameters and completeness

Motivated by the properties of known MIVCs, we devise selection criteria (Sect. 3.3) in order to identify the most prominent MIVCs from observations. We define IVCs by $20\,\mathrm{km\,s^{-1}} \leq |v_\mathrm{LSR}| \leq 100\,\mathrm{km\,s^{-1}}$ and $|b| > 20°$. In the following we discuss how these two criteria bias the identified population of Galactic IVCs. For this we consider a typical Galactic fountain as simulated by Melioli et al. (2008). In their model the fountain ejects $\sim 2.5 \times 10^5\,\mathrm{M_\odot}$ up to scale heights of $z \simeq 2$ kpc. The maximum downward motion (back onto the disk) is $v_z \simeq -100\,\mathrm{km s^{-1}}$.

Matching these characteristics, we adopt a plane-parallel slab of fountain material with $|z| = 2$ kpc and $|v_z| = 100\,\mathrm{km s^{-1}}$ down onto the disk all over the Milky Way. Due to symmetry, both cases of $z = \pm 2$ kpc are identical. These considerations are similar to Schwarz & de Boer (2004). We study the dependency of the observable Galactic latitude coordinate b and of the projected vertical velocity v_z^proj on the heliocentric distance x in one dimension (Fig. 7).

Analytically, at a heliocentric distance of $x \simeq 5.5$ kpc the considered fountain ejecta would be observed at $b \simeq 20°$ with $v_z^\mathrm{proj} \simeq -34\,\mathrm{km s^{-1}}$. At $x \simeq 9.8$ kpc one gets $b \simeq 12°$ and $v_z^\mathrm{proj} \simeq -20\,\mathrm{km s^{-1}}$. Hence, for our search the global population of IVCs of the Milky Way is restricted most by the latitude limit of $|b| > 20°$. The situation is even more severe for the MIVCs Draco, IVC 135, and IVC 210, which are located at $z \lesssim 0.5$ kpc and are observable only within $x \simeq 1.4$ kpc.

With our search parameters we trace approximately a cylindrical volume of the Milky Way with a radius of ~5.5 kpc and

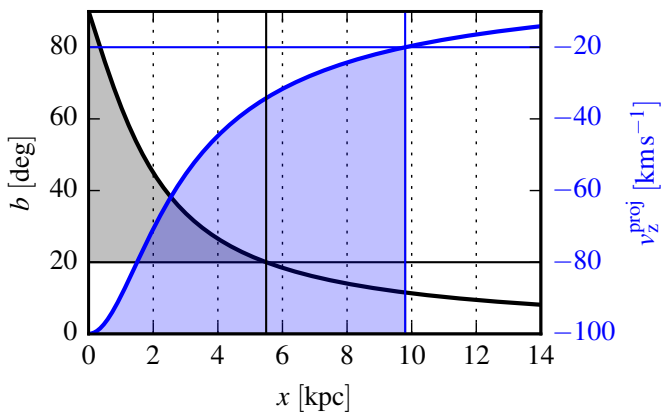

Fig. 7: Dependency of observable Galactic latitude b (black) and projected vertical velocity v_z^{proj} (blue) on heliocentric distance x for a plane-parallel slab of fountain objects at vertical scale height $z = +2$ kpc with a downward motion of $v_z = -100\,\mathrm{km s^{-1}}$. The 1D heliocentric distance x is measured within the plane of the disk. The vertical and horizontal lines mark the limits of our search for MIVCs of $20\,\mathrm{km s^{-1}} \leq |v_{LSR}| \leq 100\,\mathrm{km s^{-1}}$ and $|b| > 20°$. The coloured areas mark the observable parameter spaces.

thickness of 2×2 kpc, which is two times the height of the plane-parallel slab. We approximate the volume in our Galaxy in which star formation and fountain activity is expected to occur by the largest Galactocentric radius of high-mass star formation of ~16 kpc (Reid et al. 2009). Comparing these volumes, we find that our search may only target ~12% of the volume of interest in the Milky Way.

Extrapolating from the local MIVC population to the entire Galaxy, this yields a global H_2 inflow rate from MIVCs of $\dot{M}_{H_2} \simeq 0.05\,M_\odot\,yr^{-1} - 0.17\,M_\odot\,yr^{-1}$. Similarly, the extrapolated upper total H I and H_2 inflow rate from IVCs is $\dot{M}_H \simeq 1.3\,M_\odot\,yr^{-1} - 4.3\,M_\odot\,yr^{-1}$. Despite the considerable uncertainties in these estimates, we can draw two major conclusions from this result.

1. The total in-fall of atomic and molecular material in the form of IVC gas onto the Milky Way Galaxy as a whole may account for the entire inflow that is required for sustaining the current Galactic star formation rate.
2. A vertical scale height of $h_z \lesssim 0.5$ kpc appears to be more plausible for the class of MIVCs. Larger heights lead to unrealistic high inflow rates, even more since there are additional fuelling sources (Putman et al. 2012). This further supports the idea that MIVCs constitute a late stage in the Galactic fountain cycle. Thus, IVCs may turn molecular when they reach the disk-halo interface during their descent. Here, the environmental pressure is sufficiently high to form high density and high column density environments allowing the rapid formation of molecules and the protection against dissociating radiation (Röhser et al. 2014, their Fig. 14).

7.2. Comparison with Reach et al. (1998)

The latest all-sky study of the FIR excess emission was performed by Reach et al. (1998). Today, we analyse significantly improved data in H I and the FIR. This is one of the main reasons why we identify many more FIR excess objects.

The most important difference between our analysis and that of Reach et al. (1998) is that they fit a single component model integrated over $-100\,\mathrm{km s^{-1}} \leq v_{LSR} \leq +100\,\mathrm{km s^{-1}}$. Hence, they do not consider the radial velocity information. Furthermore, Reach et al. fit the HI-FIR correlation in cells with radius of 10° on a regular grid with 10° spacing. Towards some fields this subdivision does not allow a robust estimation of their linear parameters, e.g. due to the presence of large molecular cloud complexes. Thus, it is worthwhile to compare our results more closely to those of Reach et al. (1998).

In Sects. 4.1 and 5.1 we quantify the statistical significance of the inferred FIR excess. Using these values on the northern Galactic hemisphere at $b > 20°$, we find 694 statistically significant FIR excess objects that have angular sizes larger than a GASS beam and 232 objects that are larger than a LAB beam of $36'$ (Kalberla et al. 2005). The LAB data comprises the Leiden-Dwingeloo H I survey (Hartmann & Burton 1997), which is used by Reach et al. (1998) as well. In comparison to the 232 objects that are reported here, Reach et al. (1998) identify 56 FIR excess objects on the northern Galactic hemisphere.

For $b < -20°$, we identify 389 statistically significant FIR excess objects that are larger than a GASS beam and 105 objects larger than a LAB beam as compared to 85 FIR excess objects reported by Reach et al. (1998).

Reach et al. give thresholds for their FIR excess derived at 100 μm of $1.0\,\mathrm{MJy sr^{-1}}$ at $|b| > 20°$ and of $0.3\,\mathrm{MJy sr^{-1}}$ at $|b| > 45°$ (compare with their Fig. 6). These thresholds measure the intrinsic scatter of their residual FIR emission. In order to quantify similar thresholds, we perform our fitting of the H I-FIR correlation data as before, but with the IRIS 100 μm data (Miville-Deschênes & Lagache 2005). We find that the positive FIR excess dominates above $\sim 0.3\,\mathrm{MJy sr^{-1}}$ for $|b| > 20°$ and above $\sim 0.2\,\mathrm{MJy sr^{-1}}$ for $|b| > 45°$. Hence, our methods and our data allow to deduce more reliable results and appear to be less affected by intrinsic variations of the H I-FIR correlation than that of Reach et al. (1998).

7.3. Differences between Galactic hemispheres

There are some notable differences between the populations of MIVC candidates on the northern and southern Galactic hemispheres, both in terms of number and distribution. On the northern hemisphere there are 184 MIVC$^-$ and only three MIVC$^+$ candidates, on the southern 31 MIVC$^-$ and 21 MIVC$^+$ candidates.

If the Galactic IVC population is connected to a Galactic fountain process (e.g. Putman et al. 2012), it is unlikely to find such a significant difference in candidate numbers between both hemispheres. The lack of high-latitude southern IVC structures has been known for a long time now (e.g. Wakker 2004) but still there is no explanation.

There is a clear lack of northern MIVC$^+$ candidates. To some degree this difference is related to the different amounts of northern IVC$^\pm$ gas: At $b > 20°$ there is about three times more total H I column density in IVCs$^-$ than in IVCs$^+$. Furthermore, the median ratio $N_{HI}^{IVC^-}/N_{HI}^{LVC}$ is about four times larger than $N_{HI}^{IVC^+}/N_{HI}^{LVC}$ at $b > 20°$. Combined, this may account for a factor of ~10 in candidate numbers. Still, this is not sufficient to explain the lack of northern MIVC$^+$ candidates since at least 10 northern MIVC$^+$ candidates would be expected.

We suggest that the lack of northern MIVC$^+$ candidates is not only related to observational biases due to the different amounts of IVC$^-$ and IVC$^+$ gas and their distribution relative to the LVC gas. Instead, there may be physical reasons for the formation and existence of MIVCs in general that are linked to the kinematics

and direction of motion of the IVCs within the Galactic fountain cycle, as argued by Röhser et al. (2014, 2016). Only inflowing objects, e.g. moving towards the Galactic disk, appear to form large amounts of molecular gas that are traceable by the H I-FIR correlation.

The distributions of the northern and southern MIVC candidates are also clearly distinct. North, the candidates are located preferentially at high Galactic latitudes well above the latitude limit of $b > 20°$. South, the candidates are found at $b > -30°$. Some southern IVC structures coherently connect to structures that extend up to the Galactic disk. This suggests that at least some of the southern IVC structures are objects of the disk and not the halo. Furthermore, at lower absolute latitudes there is typically more LVC gas. This hinders the evaluation of the southern candidates.

7.4. The negative offset on the southern Galactic hemisphere

The H I-τ correlations on the northern and southern Galactic hemispheres are fitted the exact same way. However south, a negative offset in the FIR model is obtained (Table 2). Such a negative offset is unphysical since there is no negative FIR emission.

The only difference in methodology regards the masking of the Magellanic System on the southern hemisphere. This masking, in fact, alleviates the issue slightly. Hence, this offset indicates that the modelled H I-τ correlation is too steep, which suggests some bias that is introduced by the distribution of gas and dust on the southern Galactic hemisphere.

This offset might be related to the spatial offset of the Sun above the Galactic plane of 20.5 ± 3.5 pc (Humphreys & Larsen 1995). This height is a significant fraction of the molecular and cold atomic gas in our Galaxy (e.g. Kalberla 2003, his Table 3). Hence, there should be more cold and dense gas towards the southern than towards the northern Galactic hemisphere. This is consistent with our H I data. The total H I column density at $b < -20°$ is ∼23% larger than at $b > 20°$.

Furthermore, there is a correlation of mid-plane pressure and the amount of molecular gas in the disk of galaxies (Wong & Blitz 2002; Mac Low & Glover 2012). This suggests that in the innermost plane, where the vertical pressure is highest, the atomic hydrogen is most efficiently converted into molecular hydrogen. Hence, there may be more molecular gas at lower H I column densities on the southern Galactic hemisphere, which causes the slight bias in the southern H I-τ correlation.

8. Summary

In this paper we study the IVC population of the Milky Way and its FIR properties by correlating the H I and FIR emission at Galactic latitudes $|b| > 20°$. The recent H I single dish surveys EBHIS and GASS are complemented by the dust model obtained from *Planck* FIR data. This new data set allows an exceptional analysis of global ISM properties of the Milky Way.

The H I and FIR data is correlated at the angular resolution of GASS of $\theta \simeq 16.1'$. By subtracting the FIR emission associated with the atomic gas, we derive H_2 column densities across the sky with the focus on the molecular content of IVCs and on the search for molecular IVCs (MIVCs). We define MIVCs from observables obtained from the H I and FIR data only.

The all-sky H_2 maps (Figs. 2 and 5) reveal a multitude of small FIR excess objects that are not apparent in previous studies of the large-scale FIR emission and excess (e.g. Reach et al. 1998). This stresses the wealth of information obtained by the new all-sky survey data.

We retrieve all previously known MIVCs except for a single one, which is not identified due to our velocity selection between LVC and IVC gas. In total, we identify 239 MIVC candidates on both Galactic hemispheres for both negative and positive radial velocities as compiled in Tables 5 and 6. If these candidates are real MIVCs, one should be able to detect associated ^{12}CO(1→0) emission, although during the initial stages of formation CO-dark gas may dominate the H_2 content of a molecular cloud (Wolfire et al. 2010). The existing CO large-scale surveys fail to detect these objects.

The numbers and distributions of candidates differ strongly between both hemispheres and between the two radial velocity regimes: There are many more candidates found on the northern hemisphere with negative radial velocities. Such a clear dichotomy between north and south is unexpected assuming that the IVC gas is related to a Galactic fountain process. The lack of MIVC candidates with positive radial velocities appears not to be accounted for by a different amount and distribution of LVC and IVC gas. Instead, the formation of MIVCs may be related to physical mechanisms that are connected to the inflow of the clouds onto the Galactic disk. The association of HVCs with MIVC candidates is only valid for a few objects, most notably for Draco and IVC 135, for which a possible interaction between the MIVCs and HVCs has been explicitly mentioned before (Herbstmeier et al. 1993; Moritz et al. 1998; Weiß et al. 1999; Lenz et al. 2015).

The MIVC samples appear to be compatible with a model of Galactic rotation that contains radial, vertical, and lagging velocity components for different scale heights and latitudes. This may suggest that the sample is associated with Galactic rotation in the disk and some fraction of these objects are very likely connected to Galactic fountain processes within the Galactic disk.

The estimated maximum inflow rate derived from our analysis of IVCs in the local Galactic environment is $\sim 0.52\,M_\odot\,yr^{-1}$. We apply a latitude limit of $|b| > 20°$, which allows to probe only ∼10% of the volume of the Milky Way, in which IVCs are expected to be located. Extrapolating from the local IVC population to the entire Milky Way, the in-falling atomic and molecular IVC gas may account for the major fraction of the matter inflow onto our Galaxy. We derive plausible IVC inflow rates for vertical distributions with scale heights of $h_z \lesssim 0.5$ kpc. Larger heights exceed the expected mass inflow by far, suggesting that the class of MIVCs constitutes a late stage during the descent in the Galactic fountain cycle.

Future studies of the Galactic IVC population should focus on lower latitudes, for which, however, the H I-FIR correlation gets less and less clear due to blending of many emission components along the lines-of-sight. Sophisticated modelling approaches are required to extend the traceable volume in order to retrieve a more complete picture of the Galactic fountain and halo material in the Milky Way.

Acknowledgements. The authors thank the Deutsche Forschungsgemeinschaft (DFG) for financial support under the research grant KE757/11-1. The work is based on observations with the 100 m telescope of the MPIfR (Max-Planck-Institut für Radioastronomie) at Effelsberg. The Planck satellite is operated by the European Space Agency. The development of Planck has been supported by: ESA; CNES and CNRS/INSU-IN2P3-INP (France); ASI, CNR, and INAF (Italy); NASA and DoE (USA); STFC and UKSA (UK); CSIC, MICINN and JA (Spain); Tekes, AoF and CSC (Finland); DLR and MPG (Germany); CSA (Canada); DTU Space (Denmark); SER/SSO (Switzerland); RCN (Norway); SFI (Ireland); FCT/MCTES (Portugal); and PRACE (EU). Some figures have been prepared with the Kapteyn package (Terlouw & Vogelaar 2015). T. R. is a member of the International Max Planck Research School (IMPRS) for Astronomy

and Astrophysics at the Universities of Bonn and Cologne as well as of the Bonn-Cologne Graduate School of Physics and Astronomy (BCGS).

References

Akaike, H. 1974, Automatic Control, IEEE Transactions on, 19, 716
Alibés, A., Labay, J., & Canal, R. 2001, A&A, 370, 1103
Benjamin, R. A., Venn, K. A., Hiltgen, D. D., & Sneden, C. 1996, ApJ, 464, 836
Boulanger, F., Abergel, A., Bernard, J.-P., et al. 1996, A&A, 312, 256
Brand, J. & Blitz, L. 1993, A&A, 275, 67
Bregman, J. N. 1980, ApJ, 236, 577
Brüns, C., Kerp, J., Staveley-Smith, L., et al. 2005, A&A, 432, 45
Calabretta, M. R. & Greisen, E. W. 2002, A&A, 395, 1077
Chomiuk, L. & Povich, M. S. 2011, AJ, 142, 197
Dame, T. M., Hartmann, D., & Thaddeus, P. 2001, ApJ, 547, 792
Désert, F.-X., Bazell, D., & Blitz, L. 1990, ApJ, 355, L51
Désert, F. X., Bazell, D., & Boulanger, F. 1988, ApJ, 334, 815
Duarte-Cabral, A. & Dobbs, C. L. 2016, ArXiv e-prints
Fanciullo, L., Guillet, V., Aniano, G., et al. 2015, A&A, 580, A136
Fraternali, F. & Tomassetti, M. 2012, MNRAS, 426, 2166
Gillmon, K., Shull, J. M., Tumlinson, J., & Danforth, C. 2006, ApJ, 636, 891
Gladders, M. D., Clarke, T. E., Burns, C. R., et al. 1998, ApJ, 507, L161
Górski, K. M., Hivon, E., Banday, A. J., et al. 2005, ApJ, 622, 759
Grenier, I. A., Casandjian, J.-M., & Terrier, R. 2005, Science, 307, 1292
Hartmann, D. & Burton, W. B. 1997, Cambridge University Press, ISBN 0521471117
Heithausen, A., Weiß, A., Kerp, J., & Fritz, T. 2001, ApJ, 561, 238
Herbstmeier, U., Heithausen, A., & Mebold, U. 1993, A&A, 272, 514
Herbstmeier, U., Kalberla, P. M. W., Mebold, U., et al. 1996, A&AS, 117, 497
Hernandez, A. K., Wakker, B. P., Benjamin, R. A., et al. 2013, ApJ, 777, 19
Heyer, M. & Dame, T. M. 2015, ARA&A, 53, 583
Humphreys, R. M. & Larsen, J. A. 1995, AJ, 110, 2183
Kalberla, P. M. W. 2003, ApJ, 588, 805
Kalberla, P. M. W., Burton, W. B., Hartmann, D., et al. 2005, A&A, 440, 775
Kalberla, P. M. W. & Dedes, L. 2008, A&A, 487, 951
Kalberla, P. M. W. & Haud, U. 2015, A&A, 578, A78
Kalberla, P. M. W. & Kerp, J. 2009, ARA&A, 47, 27
Kalberla, P. M. W., McClure-Griffiths, N. M., Pisano, D. J., et al. 2010, A&A, 521, A17
Kalberla, P. M. W., Mebold, U., & Reich, W. 1980, A&A, 82, 275
Kerp, J., Winkel, B., Ben Bekhti, N., Flöer, L., & Kalberla, P. M. W. 2011, Astronomische Nachrichten, 332, 637
Lagache, G., Haffner, L. M., Reynolds, R. J., & Tufte, S. L. 2000, A&A, 354, 247
Lenz, D., Flöer, L., & Kerp, J. 2016, A&A, 586, A121
Lenz, D., Kerp, J., Flöer, L., et al. 2015, A&A, 573, A83
Mac Low, M.-M. & Glover, S. C. O. 2012, ApJ, 746, 135
Magnani, L. & Smith, A. J. 2010, ApJ, 722, 1685
Marasco, A. & Fraternali, F. 2011, A&A, 525, A134
Marasco, A., Fraternali, F., & Binney, J. J. 2012, MNRAS, 419, 1107
Marinacci, F., Binney, J., Fraternali, F., et al. 2010, MNRAS, 404, 1464
McClure-Griffiths, N. M., Pisano, D. J., Calabretta, M. R., et al. 2009, ApJS, 181, 398
Mebold, U., Cernicharo, J., Velden, L., et al. 1985, A&A, 151, 427
Mebold, U., Heithausen, A., & Reif, K. 1987, A&A, 180, 213
Melioli, C., Brighenti, F., D'Ercole, A., & de Gouveia Dal Pino, E. M. 2008, MNRAS, 388, 573
Meyerdierks, H. & Heithausen, A. 1996, A&A, 313, 929
Miville-Deschênes, M.-A., Boulanger, F., Reach, W. T., & Noriega-Crespo, A. 2005, ApJ, 631, L57
Miville-Deschênes, M.-A. & Lagache, G. 2005, ApJS, 157, 302
Miville-Deschênes, M.-A., Salomé, Q., Martin, P. G., et al. 2016, ArXiv e-prints
Moritz, P., Wennmacher, A., Herbstmeier, U., et al. 1998, A&A, 336, 682
Nidever, D. L., Majewski, S. R., Butler Burton, W., & Nigra, L. 2010, ApJ, 723, 1618
Peek, J. E. G., Heiles, C., Putman, M. E., & Douglas, K. 2009, ApJ, 692, 827
Planck Collaboration I. 2014, A&A, 571, A1
Planck Collaboration XI. 2014, A&A, 571, A11
Planck Collaboration XIII. 2014, A&A, 571, A13
Planck Collaboration XIX. 2011, A&A, 536, A19
Planck Collaboration XVII. 2014, A&A, 566, A55
Planck Collaboration XXIV. 2011, A&A, 536, A24
Planck Collaboration XXVI. 2015, ArXiv e-prints
Putman, M. E., Peek, J. E. G., & Joung, M. R. 2012, ARA&A, 50, 491
Reach, W. T., Wall, W. F., & Odegard, N. 1998, ApJ, 507, 507
Reid, M. J., Menten, K. M., Zheng, X. W., et al. 2009, ApJ, 700, 137
Richter, P., Wakker, B. P., Savage, B. D., & Sembach, K. R. 2003, ApJ, 586, 230
Rohlfs, R., Herbstmeier, U., Mebold, U., & Winnberg, A. 1989, A&A, 211, 402
Röhser, T., Kerp, J., Ben Bekhti, N., & Winkel, B. 2016, A&A, 592, A142
Röhser, T., Kerp, J., Winkel, B., Boulanger, F., & Lagache, G. 2014, A&A, 564, A71
Saul, D. R., Peek, J. E. G., & Putman, M. E. 2014, MNRAS, 441, 2266
Schwarz, U. J. & de Boer, K. S. 2004, in Astrophysics and Space Science Library, Vol. 312, High Velocity Clouds, ed. H. van Woerden, B. P. Wakker, U. J. Schwarz, & K. S. de Boer, 55
Snow, T. P. & McCall, B. J. 2006, ARA&A, 44, 367
Strasser, S. & Taylor, A. R. 2004, ApJ, 603, 560
Terlouw, J. P. & Vogelaar, M. G. R. 2015, Kapteyn Package, version 2.3, Kapteyn Astronomical Institute, Groningen, available from `http://www.astro.rug.nl/software/kapteyn/`
Wakker, B. P. 1991, A&A, 250, 499
Wakker, B. P. 2001, ApJS, 136, 463
Wakker, B. P. 2004, in Astrophysics and Space Science Library, Vol. 312, High Velocity Clouds, ed. H. van Woerden, B. P. Wakker, U. J. Schwarz, & K. S. de Boer, 25
Wakker, B. P. 2006, ApJS, 163, 282
Wakker, B. P. & Boulanger, F. 1986, A&A, 170, 84
Weiß, A., Heithausen, A., Herbstmeier, U., & Mebold, U. 1999, A&A, 344, 955
Williams, R. J., Mathur, S., Poindexter, S., Elvis, M., & Nicastro, F. 2012, AJ, 143, 82
Winkel, B., Kalberla, P. M. W., Kerp, J., & Flöer, L. 2010, ApJS, 188, 488
Winkel, B., Kerp, J., Flöer, L., et al. 2016a, A&A, 585, A41
Winkel, B., Lenz, D., & Flöer, L. 2016b, ArXiv e-prints
Wolfire, M. G., Hollenbach, D., & McKee, C. F. 2010, ApJ, 716, 1191
Wolfire, M. G., McKee, C. F., Hollenbach, D., & Tielens, A. G. G. M. 1995, ApJ, 453, 673
Wolfire, M. G., McKee, C. F., Hollenbach, D., & Tielens, A. G. G. M. 2003, ApJ, 587, 278
Wong, T. & Blitz, L. 2002, ApJ, 569, 157
Ysard, N., Köhler, M., Jones, A., et al. 2015, A&A, 577, A110

Table 5: Locations of MIVC$^{\pm}$ candidates with angular sizes Ω larger than one GASS beam. The columns give the Galactic longitude l and latitude b, the radial velocity $v_{\rm LSR}$, the fitted IVC dust emissivity $\epsilon^{\rm IVC}$ and its error, the peak H_2 column density $N_{\rm H_2}^{\rm peak}$ and its error, the line width FWHM, the angular size Ω, the total HI flux $S_{\rm tot}$ within $-100\,{\rm km\,s^{-1}} \leq v_{\rm LSR} \leq -20\,{\rm km\,s^{-1}}$ or $+20\,{\rm km\,s^{-1}} \leq v_{\rm LSR} \leq +100\,{\rm km\,s^{-1}}$, the rank for the samples with negative or positive LSR velocities as determined by the significance S (Eq. 4), and the MIVC designation if it is a known cloud. If there are spectral components towards a single candidate that are separated by more than $10\,{\rm km\,s^{-1}}$, then we give these two different spectral components with individual centre velocities and line widths. If $\epsilon^{\rm IVC}$ and $N_{\rm H_2}^{\rm peak}$ are both 0.00 ± 0.00, then the candidate are not fitted because either the LVC and IVC H I column densities within $2^\circ \times 2^\circ$ around the candidate are larger than $4 \times 10^{20}\,{\rm cm^{-2}}$.

l [deg]	b [deg]	$v_{\rm LSR}$ [km s^{-1}]	$\epsilon^{\rm IVC}$ [10^{-26} cm^2]	$N_{\rm H_2}^{\rm peak}$ [10^{20} cm^{-2}]	FWHM [km s^{-1}]	Ω [deg^2]	$S_{\rm tot}$ [Jy km s^{-1}]	no.	designation
				$v_{\rm LSR} < -20\,{\rm km\,s^{-1}}$					
69.8	55.5	-25.8	0.36 ± 0.02	0.68 ± 0.21	3.7	0.11	114	108	
84.5	-36.6	-53.1	0.25 ± 0.02	2.61 ± 0.18	4.8	0.12	272	123	
84.5	-37.5	-46.5	-2.20 ± 0.30	0.10 ± 0.02	4.6	0.11	262	150	
86.0	38.4	-44.5	0.75 ± 0.01	0.35 ± 0.10	3.8	0.72	982	11	
87.9	-37.3	-45.2	-0.01 ± 0.02	30.01 ± 12.57	4.7	0.30	710	145	
89.8	38.7	-25.2	2.44 ± 0.05	1.66 ± 0.06	3.8	0.60	606	22	Draco
91.4	37.8	-23.3	1.97 ± 0.04	1.79 ± 0.08	4.3	1.05	1141	16	Draco
92.2	36.3	-25.2	1.79 ± 0.08	0.85 ± 0.09	4.7	0.10	101	106	Draco
92.3	40.0	-22.5	1.41 ± 0.07	0.82 ± 0.13	4.2	0.77	792	63	Draco
92.7	39.0	-22.7	1.03 ± 0.05	1.32 ± 0.14	4.0	0.09	89	114	Draco
92.8	36.5	-24.6	2.18 ± 0.08	0.61 ± 0.07	4.4	0.38	390	66	Draco
93.3	38.1	-25.4	0.94 ± 0.04	1.31 ± 0.11	4.2	1.00	1054	45	Draco
95.5	38.1	-24.8	1.90 ± 0.03	0.98 ± 0.05	4.3	2.95	4068	5	Draco
95.9	26.3	-36.6	0.47 ± 0.01	0.92 ± 0.19	4.9	0.12	491	42	
96.0	33.2	-25.7	0.19 ± 0.02	1.74 ± 0.46	4.5	0.14	196	129	
96.5	25.6	-41.2	0.50 ± 0.01	1.14 ± 0.20	4.8	0.13	551	54	
97.2	26.2	-32.4	0.39 ± 0.02	1.27 ± 0.43	4.5	0.35	1522	87	
97.5	25.2	-32.8	0.55 ± 0.01	0.74 ± 0.28	4.2	0.27	721	50	
97.8	26.0	-36.4	0.19 ± 0.02	2.66 ± 0.94	4.5	0.27	1164	115	
98.0	24.8	-36.5	0.61 ± 0.01	0.61 ± 0.20	4.9	0.24	388	48	
98.8	26.2	-46.6	0.22 ± 0.01	1.89 ± 0.58	4.7	0.35	986	85	
98.9	28.8	-46.8	0.41 ± 0.01	0.86 ± 0.21	4.8	0.10	244	65	
99.1	27.2	-45.5/-21.4	0.25 ± 0.01	2.16 ± 0.39	4.5/4.1	0.14	481	92	
99.2	25.7	-48.2	0.46 ± 0.01	0.65 ± 0.21	3.9	0.20	446	57	
99.6	29.3	-50.6	0.49 ± 0.01	0.56 ± 0.17	4.4	0.32	623	27	
100.6	24.6	-45.5	0.57 ± 0.01	5.16 ± 0.14	4.4	0.34	1139	37	
101.9	67.4	-30.0	0.93 ± 0.01	0.42 ± 0.09	4.0	0.32	575	18	
102.4	28.1	-29.4	0.19 ± 0.02	1.46 ± 0.50	4.5	0.38	651	120	
102.9	24.4	-55.1	1.01 ± 0.03	3.85 ± 0.16	4.5	0.62	2630	41	
103.6	22.5	-47.6	0.00 ± 0.00	0.00 ± 0.00	4.1	0.65	2004	141	
105.1	21.9	-50.9/-30.1	0.00 ± 0.00	0.00 ± 0.00	4.5/4.1	3.35	13667	138	
105.5	68.7	-29.7	0.85 ± 0.01	1.91 ± 0.08	3.6	0.76	965	12	
105.6	20.6	-22.2	0.00 ± 0.00	0.00 ± 0.00	4.8	0.20	825	139	
105.7	29.5	-29.8	0.67 ± 0.01	0.68 ± 0.13	4.2	0.48	835	33	
105.7	-24.6	-53.8/-37.2	0.00 ± 0.00	0.00 ± 0.00	4.3/4.3	1.33	4851	144	
106.2	21.3	-53.4	2.08 ± 0.57	3.43 ± 0.06	4.7	0.24	894	134	
106.6	25.9	-36.5/-32.1	0.68 ± 0.03	1.75 ± 0.41	4.0/4.6	1.21	4121	43	
106.9	30.4	-32.0	0.32 ± 0.01	1.49 ± 0.27	4.7	0.20	459	88	
106.9	27.9	-58.6	-0.38 ± 0.04	2.84 ± 0.92	4.9	0.24	625	152	
107.0	70.7	-30.8	1.07 ± 0.01	0.37 ± 0.09	3.4	0.99	1519	7	
107.1	22.3	-24.2	4.61 ± 0.44	1.36 ± 0.03	4.3	0.15	388	125	
108.0	28.3	-28.6	0.36 ± 0.06	3.37 ± 1.61	4.6	0.41	819	126	
110.9	31.5	-79.0/-21.7	0.89 ± 0.02	0.58 ± 0.10	5.0/5.0	0.37	573	36	
112.1	38.6	-49.2/-33.4	0.70 ± 0.01	0.51 ± 0.11	3.9/3.9	1.80	3065	14	
112.4	37.0	-72.4/-55.1	0.81 ± 0.02	0.32 ± 0.14	4.9/4.4	0.18	348	71	
113.0	34.3	-78.8	-0.07 ± 0.02	3.14 ± 1.67	5.0	0.09	155	149	
113.3	34.8	-77.6	0.13 ± 0.01	2.25 ± 0.75	4.3	0.12	206	128	
115.1	32.6	-26.0	1.02 ± 0.02	0.44 ± 0.08	3.4	0.09	119	79	
115.3	37.7	-75.5	0.58 ± 0.01	0.41 ± 0.15	4.6	0.47	1070	32	
116.4	36.0	-21.9	0.17 ± 0.02	2.21 ± 0.40	3.1	0.48	642	112	
116.6	32.5	-25.7	0.86 ± 0.03	2.27 ± 0.16	3.6	0.22	358	86	
116.9	35.2	-24.3	0.49 ± 0.03	0.80 ± 0.20	3.7	0.11	150	122	
117.2	35.8	-21.4	0.46 ± 0.02	0.80 ± 0.17	4.1	0.26	329	89	
118.2	40.2	-48.4	0.25 ± 0.01	1.11 ± 0.35	4.4	0.32	527	74	
118.4	-21.8	-30.9	1.76 ± 0.08	0.95 ± 0.06	4.1	0.29	632	83	
118.7	35.3	-75.0	0.24 ± 0.02	1.38 ± 0.32	4.8	0.18	224	121	

Table 5: continued.

l [deg]	b [deg]	$v_{\rm LSR}$ [km s^{-1}]	$\epsilon^{\rm IVC}$ [10^{-26} cm^2]	$N_{\rm H_2}^{\rm peak}$ [10^{20} cm^{-2}]	FWHM [km s^{-1}]	Ω [deg^2]	$S_{\rm tot}$ [Jy km s^{-1}]	no.	designation
119.0	40.5	-48.3	0.26 ± 0.01	1.08 ± 0.34	4.7	0.18	236	93	
119.5	34.8	-73.5	-0.02 ± 0.02	15.36 ± 4.34	4.5	0.20	301	147	
119.7	36.8	-50.3	0.66 ± 0.03	0.50 ± 0.11	4.6	0.18	206	101	
121.2	-22.5	-32.2	1.12 ± 0.07	8.90 ± 0.36	4.5	0.13	334	118	
121.3	-21.8	-23.7	1.46 ± 0.07	6.99 ± 0.29	4.4	0.19	588	95	
122.0	-21.1	-32.3/-27.9	0.75 ± 0.03	11.42 ± 0.25	4.8/4.1	0.45	3307	75	
122.0	30.1	-26.5	4.88 ± 0.18	1.50 ± 0.04	4.6	0.22	466	82	
122.6	29.0	-23.4	0.08 ± 0.68	72.07 ± 5.57	4.0	0.62	1452	137	
123.8	44.7	-38.3	0.73 ± 0.03	0.36 ± 0.12	4.7	0.10	107	100	
124.0	-25.1	-26.7	0.44 ± 0.03	1.27 ± 0.22	5.0	0.16	308	111	
125.1	-22.8	-53.6	0.91 ± 0.02	0.94 ± 0.10	3.7	0.27	496	44	
125.2	-20.7	-61.6/-24.4	1.30 ± 0.01	0.47 ± 0.07	4.3/4.4	4.37	16345	1	
125.2	-25.6	-27.2	0.92 ± 0.03	0.68 ± 0.10	4.5	0.13	208	80	
126.6	-27.8	-53.2	0.65 ± 0.01	0.61 ± 0.17	4.9	0.22	427	55	
127.8	-20.3	-25.1	1.19 ± 0.01	0.33 ± 0.08	4.9	0.19	777	26	
128.7	29.7	-30.4	0.34 ± 0.02	1.45 ± 0.32	4.7	0.17	239	116	
129.1	29.2	-30.7	0.54 ± 0.03	1.09 ± 0.20	3.6	0.09	118	110	
129.3	-21.4	-57.0	0.76 ± 0.01	1.29 ± 0.13	4.5	0.24	818	38	
131.1	51.6	-49.2	0.46 ± 0.02	0.61 ± 0.16	3.6	0.12	171	107	IVC 135
132.4	26.6	-39.9	2.04 ± 0.03	0.36 ± 0.06	4.0	0.19	332	39	
132.5	53.3	-48.8	1.02 ± 0.02	0.27 ± 0.07	3.8	0.27	370	34	IVC 135
133.4	23.4	-55.6	0.00 ± 0.00	0.00 ± 0.00	4.1	0.31	880	140	
133.9	34.4	-62.0	1.00 ± 0.02	0.26 ± 0.08	4.8	0.18	210	62	
135.2	51.4	-48.9	1.40 ± 0.01	0.26 ± 0.06	3.8	3.45	5897	2	IVC 135
135.3	36.5	-42.2	0.96 ± 0.03	0.45 ± 0.12	5.0	0.19	236	78	
136.0	54.6	-48.8	1.70 ± 0.02	0.29 ± 0.09	3.7	5.75	10355	3	IVC 135
136.4	-25.5	-63.0	1.13 ± 0.02	0.78 ± 0.10	4.4	0.20	416	59	
136.8	57.8	-47.4	0.81 ± 0.01	0.37 ± 0.11	3.6	0.80	1283	15	IVC 135
138.0	-20.4	-57.6	1.14 ± 0.02	0.28 ± 0.10	4.4	0.73	1752	23	
142.6	40.0	-52.8	2.10 ± 0.06	2.25 ± 0.12	4.5	0.16	251	73	
142.9	39.5	-55.3	2.06 ± 0.06	3.23 ± 0.11	2.9	0.14	235	84	
143.8	40.0	-54.1	1.82 ± 0.05	3.64 ± 0.11	4.5	0.71	1201	35	
144.7	39.0	-55.1	2.32 ± 0.09	2.45 ± 0.14	4.4	0.36	539	70	
145.2	44.4	-46.8	-0.11 ± 0.06	5.32 ± 1.88	4.4	0.28	319	148	
145.5	40.0	-56.1	-0.55 ± 0.09	2.43 ± 0.79	4.3	1.36	2206	153	
145.7	43.4	-51.0	0.23 ± 0.06	7.83 ± 1.11	4.5	0.23	342	133	
146.3	36.1	-58.0	2.33 ± 0.06	0.92 ± 0.08	4.3	0.29	350	61	
147.6	38.2	-57.6	2.03 ± 0.12	2.04 ± 0.26	4.0	1.70	2741	52	
149.8	67.5	-53.7	0.18 ± 0.01	2.44 ± 0.41	4.3	0.28	309	96	
150.4	33.6	-53.8	0.64 ± 0.03	1.04 ± 0.19	4.7	0.11	182	104	
151.7	40.8	-62.7	1.40 ± 0.03	0.91 ± 0.09	3.4	0.22	241	58	
151.7	37.3	-59.8	2.83 ± 0.12	2.45 ± 0.15	4.4	0.40	627	72	
153.6	32.8	-54.0	0.96 ± 0.03	0.55 ± 0.14	4.7	0.40	671	51	
159.0	38.4	-54.1	1.02 ± 0.08	2.01 ± 0.34	4.1	0.18	300	117	
160.0	35.6	-54.4	1.52 ± 0.07	1.24 ± 0.18	3.6	0.17	323	102	
160.7	35.7	-56.0	1.63 ± 0.06	0.92 ± 0.14	4.6	0.34	573	67	
161.0	61.2	-24.3	0.97 ± 0.04	0.25 ± 0.08	4.4	0.12	125	99	
175.1	70.1	-27.0	0.98 ± 0.04	0.28 ± 0.09	4.5	0.09	109	103	
196.9	51.3	-21.7	0.79 ± 0.03	0.28 ± 0.10	4.8	0.28	305	77	
201.0	56.1	-52.3	0.47 ± 0.01	0.38 ± 0.12	3.7	0.13	256	69	
202.0	56.2	-50.3	0.61 ± 0.01	0.38 ± 0.09	4.3	0.17	288	40	
202.9	67.6	-40.6	0.54 ± 0.02	0.45 ± 0.12	4.3	0.15	196	81	
203.1	55.0	-49.0	0.58 ± 0.01	0.37 ± 0.12	4.5	0.73	1573	13	
208.8	48.3	-50.8	0.82 ± 0.03	0.38 ± 0.13	3.9	0.22	234	91	
208.9	44.6	-39.5	0.18 ± 0.03	5.47 ± 0.54	4.4	0.15	169	131	
209.3	47.8	-48.9	1.46 ± 0.03	0.18 ± 0.06	3.9	0.15	207	64	
209.9	61.5	-39.7	0.71 ± 0.02	0.57 ± 0.13	4.8	0.09	152	97	IVC 210
210.0	46.7	-34.5	1.30 ± 0.02	0.25 ± 0.06	4.9	0.16	226	56	
210.7	61.0	-34.3	0.75 ± 0.02	0.55 ± 0.10	4.6	0.30	438	49	IVC 210
210.8	46.5	-43.8	1.32 ± 0.02	0.23 ± 0.08	4.6	0.20	275	47	
211.1	45.5	-46.0/-32.9	0.93 ± 0.02	0.48 ± 0.11	4.9/4.2	0.90	1083	24	
211.4	63.1	-40.4	1.05 ± 0.01	0.95 ± 0.08	4.0	1.53	2635	6	IVC 210
213.3	43.3	-34.0	0.47 ± 0.02	0.63 ± 0.17	4.3	0.13	152	105	
214.3	62.3	-39.2	0.88 ± 0.01	0.38 ± 0.08	4.2	0.28	310	28	IVC 210
215.1	37.2	-48.7/-21.6	1.04 ± 0.01	0.32 ± 0.10	4.4/4.3	0.54	824	9	
215.9	38.1	-27.7	1.13 ± 0.02	0.29 ± 0.10	4.3	0.42	654	20	

Table 5: continued.

l [deg]	b [deg]	$v_{\rm LSR}$ [km s^{-1}]	$\epsilon^{\rm IVC}$ [10^{-26} cm^2]	$N_{\rm H_2}^{\rm peak}$ [10^{20} cm^{-2}]	FWHM [km s^{-1}]	Ω [deg^2]	$S_{\rm tot}$ [Jy km s^{-1}]	no.	designation
216.1	39.1	-31.9	1.19 ± 0.02	0.30 ± 0.08	4.2	0.59	633	19	
216.5	37.2	-30.5	1.08 ± 0.01	0.66 ± 0.09	4.8	0.34	472	8	
219.1	42.0	-34.2	0.63 ± 0.02	0.53 ± 0.16	4.3	0.46	543	60	
219.2	43.6	-38.6/-28.3	0.77 ± 0.02	0.71 ± 0.16	4.4/4.8	0.89	1362	17	
220.6	51.9	-34.8	0.01 ± 0.03	42.08 ± 14.39	4.7	0.21	267	136	
231.4	80.7	-20.2	0.60 ± 0.01	0.40 ± 0.08	3.9	0.23	372	53	
246.1	73.0	-26.0	0.23 ± 0.03	11.95 ± 0.65	4.1	1.50	2959	90	
251.6	74.8	-30.7	0.32 ± 0.06	9.96 ± 0.89	4.2	0.16	160	132	
251.9	77.9	-43.6	-0.27 ± 0.02	0.98 ± 0.35	4.8	0.09	120	151	
255.6	52.9	-33.4	-0.01 ± 0.01	28.43 ± 11.68	4.6	0.24	355	146	
256.2	76.6	-28.3	0.73 ± 0.02	0.44 ± 0.13	4.0	1.09	1580	29	
259.4	53.9	-29.3	0.44 ± 0.01	0.70 ± 0.21	3.7	0.14	303	76	
260.0	79.0	-30.1	0.44 ± 0.03	1.12 ± 0.22	4.5	0.12	122	119	
260.5	80.6	-29.5	0.31 ± 0.05	1.26 ± 0.50	4.7	0.30	368	127	
262.5	78.0	-31.5	0.04 ± 0.02	8.60 ± 2.84	4.1	0.39	501	135	
265.0	79.5	-30.5	0.29 ± 0.03	1.56 ± 0.40	4.4	0.42	451	113	
265.5	80.6	-29.4	0.48 ± 0.04	0.74 ± 0.31	3.6	0.11	127	124	
266.8	52.8	-32.8	0.97 ± 0.02	0.53 ± 0.17	4.3	0.67	1407	21	
267.3	81.3	-30.2	0.71 ± 0.04	0.74 ± 0.19	4.5	0.24	256	98	
267.7	53.1	-30.8	0.89 ± 0.03	0.66 ± 0.21	4.2	0.10	222	94	
267.8	52.7	-22.4	0.87 ± 0.03	0.62 ± 0.21	4.6	0.23	440	68	
269.3	60.8	-42.1	0.17 ± 0.02	1.10 ± 0.42	4.6	0.13	135	130	
276.3	82.6	-30.1	0.59 ± 0.04	0.78 ± 0.19	4.8	0.14	146	109	
278.7	51.5	-31.9	0.81 ± 0.01	0.72 ± 0.09	4.1	1.50	4357	4	
279.6	50.8	-32.0	0.68 ± 0.01	0.70 ± 0.15	3.4	0.15	249	25	
283.9	54.9	-31.7	0.45 ± 0.01	1.01 ± 0.14	4.4	0.11	344	46	G 283.9+54.9
284.0	51.7	-26.8	0.58 ± 0.02	1.28 ± 0.32	4.3	1.77	3248	31	
288.4	53.0	-24.2	0.91 ± 0.02	1.35 ± 0.15	4.3	1.89	3274	10	G 288.4+53.2
304.5	-23.7	-34.0/-26.7	0.00 ± 0.00	0.00 ± 0.00	4.2/4.4	0.75	2344	143	
310.6	-20.2	-31.6	0.00 ± 0.00	0.00 ± 0.00	4.9	0.20	817	142	
325.7	52.1	-42.9	1.25 ± 0.02	0.26 ± 0.06	4.8	0.20	196	30	
				$v_{\rm LSR} > +20$ km s^{-1}					
25.8	-21.3	20.7	0.00 ± 0.00	0.00 ± 0.00	4.9	0.13	388	15	
29.3	-20.1	24.1	0.00 ± 0.00	0.00 ± 0.00	4.4	0.24	882	14	
225.5	-20.5	29.8	0.90 ± 0.05	0.75 ± 0.24	4.7	0.09	169	11	
226.3	-22.8	32.9	0.95 ± 0.03	0.43 ± 0.12	3.0	0.29	341	7	
234.5	-32.9	21.5	2.10 ± 0.02	0.13 ± 0.04	3.9	0.50	473	1	
238.1	-20.1	39.4	0.97 ± 0.01	0.25 ± 0.09	4.5	0.19	390	4	
240.0	-22.1	46.7	0.71 ± 0.01	0.51 ± 0.14	3.8	0.19	301	5	
240.2	-20.9	21.8/42.7	0.66 ± 0.02	0.54 ± 0.17	4.1/4.8	1.03	1814	3	
241.7	-20.2	24.4	0.47 ± 0.03	2.01 ± 0.35	4.7	0.24	340	10	
254.2	-20.4	37.3	0.53 ± 0.05	1.51 ± 0.54	4.1	2.07	4585	6	
255.8	-26.0	27.0	0.49 ± 0.03	1.25 ± 0.42	4.1	0.33	473	8	
256.0	-20.5	33.2	0.04 ± 0.02	9.95 ± 3.81	4.2	0.73	2348	13	
256.8	-25.9	27.4	0.13 ± 0.02	3.36 ± 1.43	3.8	0.44	692	12	
257.2	-22.0	25.1	-0.20 ± 0.03	4.82 ± 1.58	4.2	3.88	8962	17	
257.5	-28.1	27.4	0.33 ± 0.02	1.26 ± 0.17	4.8	0.19	200	9	
258.2	-21.4	23.3	1.13 ± 0.01	0.34 ± 0.10	4.7	0.13	252	2	
258.5	-24.5	21.6	-0.32 ± 0.02	1.04 ± 0.36	3.9	0.56	865	18	
259.7	35.0	23.9	0.00 ± 0.00	0.00 ± 0.00	4.7	0.12	381	16	

Table 6: Locations of MIVC$^{\pm}$ candidates with angular sizes Ω smaller than one GASS beam. The columns give the Galactic longitude l and latitude b, the radial velocity $v_{\rm LSR}$, the fitted IVC dust emissivity $\epsilon^{\rm IVC}$ and its error, the peak H_2 column density $N_{\rm H_2}^{\rm peak}$ and its error, the line width FWHM, the angular size Ω, the total HI flux $S_{\rm tot}$ within $-100\,{\rm km\,s^{-1}} \le v_{\rm LSR} \le -20\,{\rm km\,s^{-1}}$ or $+20\,{\rm km\,s^{-1}} \le v_{\rm LSR} \le +100\,{\rm km\,s^{-1}}$, the rank for the samples with negative or positive LSR velocities as determined by the significance S (Eq. 4), and the MIVC designation if it is a known cloud. If there are spectral components towards a single candidate that are separated by more than $10\,{\rm km\,s^{-1}}$, then we give these two different spectral components with individual centre velocities and line widths. If $\epsilon^{\rm IVC}$ and $N_{\rm H_2}^{\rm peak}$ are both 0.00 ± 0.00, then the candidate are not fitted because either the LVC and IVC H I column densities within $2^\circ \times 2^\circ$ around the candidate are larger than $4 \times 10^{20}\,{\rm cm^{-2}}$.

l [deg]	b [deg]	$v_{\rm LSR}$ [km s^{-1}]	$\epsilon^{\rm IVC}$ [10^{-26} cm^2]	$N_{\rm H_2}^{\rm peak}$ [10^{20} cm^{-2}]	FWHM [km s^{-1}]	Ω [deg^2]	$S_{\rm tot}$ [Jy km s^{-1}]	no.	designation
				$v_{\rm LSR} < -20\,{\rm km\,s^{-1}}$					
70.0	54.8	-22.7	0.58 ± 0.02	0.42 ± 0.13	3.8	0.012	12.2	28	
84.3	-37.2	-46.4	0.98 ± 0.21	0.96 ± 0.06	4.6	0.003	16.0	55	
85.2	-36.8	-48.8	0.13 ± 0.02	4.78 ± 0.28	4.6	0.056	25.8	49	
86.1	-38.1	-42.5	0.29 ± 0.01	4.24 ± 0.18	5.0	0.018	16.3	23	
87.2	57.8	-38.9	0.21 ± 0.01	1.21 ± 0.31	4.3	0.041	5.0	17	
93.1	23.2	-35.6	0.81 ± 0.02	0.59 ± 0.09	4.7	0.068	12.7	7	
96.0	25.1	-35.1	0.57 ± 0.01	0.62 ± 0.19	4.4	0.015	19.8	13	
96.2	-30.6	-53.0	-0.26 ± 0.07	5.71 ± 1.15	4.7	0.021	6.6	60	
98.1	21.9	-47.3	0.35 ± 0.05	3.07 ± 0.30	3.8	0.074	19.8	40	
100.1	27.8	-51.1	0.30 ± 0.01	1.48 ± 0.32	4.6	0.009	29.4	24	
105.1	34.0	-52.5	0.47 ± 0.02	0.90 ± 0.20	3.5	0.029	16.2	22	
106.1	-23.8	-35.8	0.00 ± 0.00	0.00 ± 0.00	4.3	0.009	30.0	58	
107.0	-24.4	-56.2	0.00 ± 0.00	0.00 ± 0.00	3.4	0.018	41.7	59	
108.3	35.5	-70.7	0.15 ± 0.01	1.78 ± 0.45	4.5	0.032	18.1	41	
108.7	-33.4	-53.4	0.69 ± 0.01	0.54 ± 0.10	4.7	0.032	8.1	6	
108.7	25.4	-28.8	0.45 ± 0.09	3.24 ± 1.01	4.9	0.074	18.0	46	
112.2	37.6	-36.1	0.78 ± 0.02	0.43 ± 0.14	4.7	0.015	21.1	20	
113.6	37.3	-54.4	0.74 ± 0.01	0.48 ± 0.13	4.4	0.024	24.6	10	
113.6	34.0	-79.3	0.29 ± 0.02	0.76 ± 0.36	4.3	0.029	17.6	27	
113.7	34.9	-71.8	0.39 ± 0.01	0.61 ± 0.21	4.8	0.003	18.5	43	
114.0	34.6	-76.7	0.45 ± 0.01	0.53 ± 0.18	4.7	0.059	20.7	9	
116.2	56.6	-65.9	0.43 ± 0.03	0.61 ± 0.23	4.2	0.038	6.1	25	
122.4	30.0	-26.6	4.06 ± 0.26	2.34 ± 0.07	4.8	0.027	20.4	34	
126.3	-25.6	-58.3	1.08 ± 0.02	0.53 ± 0.08	4.8	0.027	32.1	11	
127.0	-28.3	-21.2	0.81 ± 0.02	0.66 ± 0.13	4.9	0.015	28.3	16	
127.3	-26.4	-36.6	0.97 ± 0.02	0.22 ± 0.10	4.6	0.074	25.8	3	
130.2	39.3	-20.8	-0.84 ± 0.04	0.40 ± 0.13	4.5	0.009	12.6	62	
130.4	51.3	-47.6	0.39 ± 0.02	0.73 ± 0.22	4.4	0.080	72.2	19	IVC 135
141.8	41.1	-48.5	2.30 ± 0.03	0.91 ± 0.07	4.5	0.044	23.2	4	
144.5	42.2	-51.0	0.51 ± 0.05	2.89 ± 0.57	4.6	0.009	17.6	52	
150.7	40.3	-59.2	0.59 ± 0.07	3.63 ± 0.45	4.3	0.056	38.4	39	
151.1	32.6	-49.4	0.94 ± 0.04	0.65 ± 0.14	4.0	0.012	22.4	33	
152.3	39.7	-52.5	1.67 ± 0.09	0.70 ± 0.16	3.2	0.003	52.6	50	
154.6	38.7	-59.8	1.33 ± 0.08	1.97 ± 0.27	3.8	0.015	59.0	37	
163.0	34.9	-59.1	0.89 ± 0.01	0.39 ± 0.09	3.8	0.062	34.2	1	
176.5	27.8	-25.5	0.23 ± 0.02	1.07 ± 0.49	4.1	0.015	38.1	44	
202.2	53.8	-20.9	0.73 ± 0.01	0.37 ± 0.09	4.8	0.018	49.6	8	
204.0	39.5	-37.1	0.82 ± 0.02	0.50 ± 0.10	3.6	0.009	9.1	18	
206.2	48.6	-39.8	1.31 ± 0.03	0.29 ± 0.05	4.1	0.003	15.7	29	
206.5	48.6	-43.2	1.43 ± 0.02	0.24 ± 0.04	4.7	0.080	14.2	2	
209.0	49.6	-47.6	0.22 ± 0.02	1.24 ± 0.33	4.5	0.032	12.1	42	
209.3	49.3	-47.6	0.23 ± 0.02	1.45 ± 0.37	4.5	0.018	10.5	48	
211.8	44.8	-33.1	0.99 ± 0.02	0.35 ± 0.10	3.2	0.003	25.3	31	
213.2	61.9	-35.6	0.82 ± 0.02	0.73 ± 0.11	4.5	0.009	14.7	21	IVC 210
213.5	39.0	-38.5	-0.12 ± 0.02	2.12 ± 0.69	5.0	0.038	3.7	61	
218.6	41.4	-33.8	0.31 ± 0.03	1.34 ± 0.40	4.6	0.065	2.1	30	
252.9	76.1	-25.8	0.84 ± 0.02	1.11 ± 0.10	4.8	0.029	42.6	15	
254.4	77.1	-25.8	0.66 ± 0.02	0.45 ± 0.15	5.0	0.053	54.6	12	
256.1	79.1	-29.1	0.20 ± 0.04	1.82 ± 0.60	3.9	0.006	39.3	54	
256.8	73.1	-30.6	0.82 ± 0.06	3.09 ± 0.31	3.7	0.003	87.5	53	
258.3	78.1	-28.6	0.10 ± 0.03	4.96 ± 1.37	2.8	0.080	45.7	51	
258.7	76.0	-28.5	1.11 ± 0.02	0.39 ± 0.09	4.4	0.050	69.0	5	
259.2	49.7	-29.4	0.38 ± 0.01	0.70 ± 0.22	4.9	0.009	16.4	35	
260.5	50.3	-23.5	0.35 ± 0.02	0.90 ± 0.30	4.8	0.029	15.9	26	
269.4	81.7	-29.2	0.54 ± 0.04	0.94 ± 0.27	4.9	0.024	41.7	36	
271.0	75.4	-39.9	0.09 ± 0.01	5.69 ± 0.82	4.1	0.029	58.2	47	

Table 6: continued.

l [deg]	b [deg]	$v_{\rm LSR}$ [km s^{-1}]	$\epsilon^{\rm IVC}$ [10^{-26} cm^2]	$N_{\rm H_2}^{\rm peak}$ [10^{20} cm^{-2}]	FWHM [km s^{-1}]	Ω [deg^2]	$S_{\rm tot}$ [Jy km s^{-1}]	no.	designation
279.1	85.2	-28.3	0.16 ± 0.03	2.11 ± 0.45	4.3	0.062	55.1	45	
284.4	52.6	-29.1	0.69 ± 0.02	1.11 ± 0.22	3.6	0.003	24.7	38	
286.2	52.6	-23.7	1.35 ± 0.03	0.59 ± 0.10	3.6	0.021	18.6	14	G 288.4+53.2
303.2	-23.9	-27.7	0.00 ± 0.00	0.00 ± 0.00	4.4	0.047	15.9	56	
312.5	54.6	-48.0	0.75 ± 0.03	0.44 ± 0.12	3.8	0.012	47.4	32	
316.0	-20.6	-26.0	0.00 ± 0.00	0.00 ± 0.00	4.9	0.006	76.1	57	
$v_{\rm LSR} > +20$ km s^{-1}									
25.2	-19.8	25.1	0.00 ± 0.00	0.00 ± 0.00	5.0	0.021	79.6	6	
25.5	-20.8	23.0	0.00 ± 0.00	0.00 ± 0.00	4.8	0.038	103.9	5	
254.1	-21.7	36.8	0.61 ± 0.03	1.33 ± 0.34	4.3	0.003	57.3	4	
254.3	-23.8	22.9	0.25 ± 0.01	1.77 ± 0.41	4.9	0.029	38.4	1	
290.2	37.3	30.5	0.40 ± 0.02	1.94 ± 0.21	4.0	0.006	3.1	3	
293.0	37.6	29.0	1.06 ± 0.05	0.67 ± 0.04	4.9	0.006	2.0	2	